Heliyon 10 (2024) e23389

Contents lists available at ScienceDirect

Heliyon

journal homepage: www.cell.com/heliyon

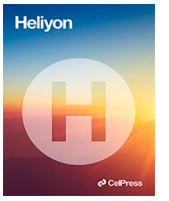

Research and optimization of hydrogen addition and EGR on the combustion, performance, and emission of the biodiesel-hydrogen dual-fuel engine with different loads based on the RSM

Zhiqing Zhang [a,b,c], Hui Liu [a,b], Youchang Li [b,*], Yanshuai Ye [a], Jie Tian [a], Jiangtao Li [a], Yuejiang Xu [a], Junshuai Lv [c]

[a] Guangxi Earthmoving Machinery Collaborative Innovation Center, Guangxi University of Science and Technology, Liuzhou 545006, China
[b] Center for Applied Mathematics of Guangxi, Yulin Normal University, Yulin 537000, China
[c] Guangxi Key Laboratory of Ocean Engineering Equipment and Technology, Beibu Gulf University, Qinzhou 535011, China

ARTICLE INFO

Keywords:
Biodiesel-hydrogen blend
Response surface methodology
Combustion characteristic
Emission characteristic
Multi-objective optimization

ABSTRACT

Pollutants produced by engines are a significant source of environmental pollution, so the study of engine emissions is very important. In this study, with CONVERGE software, a diesel engine model of the engine was produced. To better obtain the characteristic results of the engine, this was coupled with an improved chemical kinetics mechanism. Then, the results of this model were verified experimentally. Additionally, the effects of four different EGR rates on the combustion, performance, and emissions of a dual-fuel diesel engine were investigated by the verified model under different (50 %, 75 %, and 100 %) load conditions. Lastly, the brake specific fuel consumption, NO_x emission, and HC emission were optimized by the response surface methodology (RSM). The results show that the pressure, temperature, and NO_x emission in the engine's cylinder can all be reduced by raising the EGR at three different loads. Besides, the optimization results show that the engine achieves the best operating conditions at 100 % load, hydrogen fraction of 6.92 %, and EGR rate of 7.68 %.

1. Introduction

Engines are the main power source of automobiles and boats and are heavily used in the transportation sector [1]. The variety and quantity of engines have grown considerably in recent years [2]. Although the emergence of electric vehicles and fuel cell automobiles has occupied a part of the traditional engine market share in recent years, diesel-engine automobiles are still occupying a large proportion of the global market [3]. The emergence of the engines has improved people's lives to a large extent, but it has also caused a series of negative problems in terms of the environment, energy, and economy [4]. The burning of fossil fuels in engines produces a range of harmful substances, like CO, HC, NO_x, soot, and PM [5]. These harmful substances cause serious pollution to the environment and serious damage to the human respiratory and cardiovascular systems [6]. Emissions from automobiles have significantly increased in the past couple of decades [7]. Therefore, the improvement of pollutant emissions from engines is particularly important for achieving the goal of low-carbon development [8]. Thus, finding new cleaner fuels to instead of traditional fossil fuels and developing new technologies to reduce harmful gas emissions are of great importance [9]. Currently, the new clean fuel mainly includes H_2, LPG,

* Corresponding author.
E-mail address: liyc@ylu.edu.cn (Y. Li).

https://doi.org/10.1016/j.heliyon.2023.e23389
Received 3 September 2023; Received in revised form 10 November 2023; Accepted 3 December 2023
Available online 7 December 2023

Abbreviations

3D	Three dimensions
CI	compression-ignition
EGR	exhaust gas recirculation
HRR	Heat release rate
HC	Hydrocarbons
NO	Nitrogen monoxide
NO_x	Nitrogen oxides
H_2	Hydrogen gas
N_2	Nitrogen gas
KH-RT	The Rayleigh-Taylor Model and Kelvin-Helmholtz Model
PM	Fine particulate matter
BH10	90%biodiesel+10%hydrogen
LPG	liquefied petroleum gas
N_2O	Nitrous oxide
NO_2	Nitrogen dioxide
H_2O	Water
CFD	Computational fluid dynamics
RSM	Response surface methodology

biodiesel, alcohol fuels [10] and ammonia, and has also been recognized as a promising and sustainable clean fuel in recent years [11]. Among them, due to hydrogen contains no carbon atoms, the product of its full combustion is H_2O [12]. According to studies, hydrogen has been discovered to be among the cleanest combustible fuels for engines [13]. Due to its high combustion efficiency, environmentally friendly combustion products, and theoretical recyclability, the research of hydrogen has attracted a lot of attention from researchers around the world [14]. However, due to its high autoignition temperature (858 K), low cetane number, and not easy spontaneous combustion under reasonable compression ratio conditions, hydrogen is unable to be applied as a separate fuel for CI engines [15]. Research has indicated that hydrogen can be utilized in dual-fuel (diesel-hydrogen) CI engines by utilizing a tiny quantity of diesel as the fire fuel and hydrogen as the staple fuel. Besides, a good combustion characteristic can be obtained in dual-fuel mode [16].

Biodiesel is a kind of hydrophobic polymer substance, and its main component is glycerol fatty acid methyl ester [17]. The main feedstock for biodiesel is animal fats and oils, vegetable oils, or discarded edible oils, and the main extraction method at present is the ester-exchange method [18]. Biodiesel has the characteristics of being renewable, nontoxic, biodegradable, and nonflammable. Compared with traditional fossil diesel, biodiesel has a greater viscosity, higher filtration point, lower calorific value, and better lubricity [19]. With a few minor adjustments of the fuel injection system or combustion system for the diesel engine, biodiesel can be burned directly in the engine cylinder [20]. Furthermore, it can enhance the diesel engines' emission qualities and somewhat lower the emissions of polluting pollutants like PM, soot, CO, and HC [21]. In contrast with diesel fuel, biodiesel use is beneficial in reducing carbon buildup and wear and tear of key engine components [22]. However, compared to fossil diesel, biodiesel frequently has a higher viscosity, poor atomizing characteristics, high cold filtration point [23], and poor fluidity in the environment, resulting in difficult application, whereas biodiesel has both a high and a low impact on the amount of NO_x in engine exhaust. As shown by Murillo S. et al. [24], the biodiesel-diesel blend fuel was made from different proportions of cooking oils. According to the results, biodiesel has a 20 % rise in NO_x concentration. Can Ö [25]. had produced the biodiesel by cooking oil and blended it with #2 diesel fuel to obtain blended fuels B5 and B10 at 5 % and 10 %, respectively. The results showed an increase of about 8.7 % in NO_x due to the addition of biodiesel. However, lots of studies have concluded that when biodiesel content increases, NO_x emission is reduced. In addition, Hoekman and Robbins [26] summarized the factors affecting the NO_x emission content of biodiesel.

The fuel traits of biodiesel rest on the composition of fatty acids of oils and fats [27]. Study shows that compared to fossil diesel, biodiesel has a lower calorific value. Biodiesel is characterized by high viscosity and poor atomization, it is therefore believed that biodiesel combustion can be enhanced by the fuels with high calorific value and high flame propagation rate [28]. High heat value [29] and rapid flame propagation are two properties of hydrogen [30]. Additionally, hydrogen has strong diffusivity, and is simple to mix with air. Vijayaragavan et al. [31] had examined the effect of simarouba oil and hydrogen as fuels on a dual-fuel CI engine. The findings demonstrated that, in comparison to using only pure biodiesel, the engine's performance was enhanced by the addition of hydrogen. However, there was an increased trend in NO_x emission because of the hydrogen's greater temperature and flame pace. Tan et al. [32] examined the influence of the additions of hydrogen and water by multi-objective optimization method. The results concluded that when the proper amount of water and hydrogen is added, biodiesel might be employed in marine engines to produce clean, low-carbon, and efficient combustion. Therefore, to reduce the negative effects of biodiesel used in CI engines, the addition of hydrogen is employed to mix with biodiesel [33]. It is helpful for the study of biodiesel-hydrogen dual-fuel.

To decrease the harmful emissions from the engine, it is imperative to think about not only the aspect of fuel but also the aspect of technology. For diesel engines, lots of research has shown that EGR technology is one of the most useful technological means to decrease the emissions of NO_x and PM [34]. Due to the participation of exhaust gases, the concentration of oxygen entering the

cylinder is relatively low. The exhaust gases contain CO_2 and H_2O, which lower the in-cylinder temperature to some extent, thereby decreasing the production of NO_x [35]. Hitoshi Yokomura [36] carried out a study on an engine to examine the impact of EGR rate on the combustibility and emission parameters of the engine. The outcomes demonstrated that a higher EGR rate and excess air coefficient might successfully lower NO_x emission. Moreover, the outcomes of the study by Dickey et al. [37] showed that NO_x emission could be decreased by more than 50 % when the EGR rate was 15 %, and by more than 80 % when the EGR rate was 25 %. Additionally, the increased EGR may results in higher PM and HC emissions. Similarly, Kumar and Saravanan [38] examined the influence of EGR rates on diesel engines using blended fuels, the result shown that the increased EGR rate results in a lower NO_x emission.

In contrast to experimentation, optimization algorithms can optimize a vast array of engine parameters by using regression analysis in the optimization process. The RSM is usually more computationally efficient than some traditional optimization algorithms. In data analysis, RSM can forecast unmeasured data to get better findings with fewer test cycles and less time spent on analysis. Firstly, in this study, the impact of four distinct EGR rates (0 %, 5 %, 10 %, and 15 %) on a diesel engine running on a dual fuel of biodiesel and hydrogen was examined using the validated model. Then, the BSFC, NO_x emission, and HC emission were optimized by the RSM. Finally, the RME method is used to determine how varying biodiesel-to-hydrogen mixture ratios and EGR rates affect the engine's characteristics.

2. Numerical modeling and methods

2.1. Basic control equations

Air was regarded as the ideal gas in this work. The following represents the steps of detailed modeling.

2.1.1. The conservation equation

The control equations expressed using the Hamiltonian operator are as follows.

(1) The equation for the conservation of mass is [39]:

$$\frac{\partial \rho}{\partial t} + \nabla \cdot \rho \boldsymbol{U} = 0 \tag{1}$$

where $\boldsymbol{U}$ was the fluid flow velocity field; ρ was density, g/cm^3; and ∇ is the Hamiltonian operator.

(2) The equation of motion can be explained [39]:

$$\rho \frac{\partial \boldsymbol{U}}{\partial t} + \rho \boldsymbol{U} \cdot \nabla \boldsymbol{U} = -\nabla p + \nabla \cdot \left(T_{ij}\, \boldsymbol{e}_i \boldsymbol{e}_j\right) + \dot{S} \tag{2}$$

The T_{ij} is calculated as:

$$T_{ij} = \mu \left(\frac{\partial U_i}{\partial x_j} + \frac{\partial U_j}{\partial x_i}\right) + \left(\mu^{'} - \frac{2}{3}\mu\right)\left(\frac{\partial U_{\mathrm{k}}}{\partial x_{\mathrm{k}}}\, \delta_{ij}\right) \tag{3}$$

where μ is the kinetic viscosity, N·s/m^2; μ' is the expansion viscosity, mPa · s; $\boldsymbol{e}_i$ and $\boldsymbol{e}_j$ are coordinate basis vectors; δ_{ij} is the Kronecker notation; and $\dot{S}$ is the source term; p is the pressure, Pa;

(3) The equation of energy can be explained [39]:

$$\frac{\partial \rho e}{\partial t} + \rho e \nabla \cdot \boldsymbol{U} = -p \nabla \cdot \boldsymbol{U} + T_{ij} \nabla \cdot \boldsymbol{U} + \lambda \nabla \cdot \nabla T + \nabla \left(\rho D \sum_{\mathrm{m}} h_{\mathrm{m}} \nabla Y_{\mathrm{m}}\right) + \dot{S} \tag{4}$$

where D is the mass spread coefficient, cm^2/s; e is the specific inner energy, kJ/kg; λ is the heat conduction ratio, W/(m^2·k); T denotes the temperature, K; h_{m} denotes the enthalpy of component m, kJ; and Y_{m} denotes the mass fractional number of gas component m, %.

2.1.2. Gas equation of state

The density, pressure, and temperature of the gas in an engine cylinder can be determined using the gas formula of state. The formula takes the form [40]:

$$pV_{\mathrm{m}} = ZRT \tag{5}$$

where V_{m} is the molar volume and $V_{\mathrm{m}} = W/\rho$, mL/mol; p is the absolute pressure, Pa; R is the molar gas constant, cal/(K·g·mol); W is the molar mass, g/mol; Z is the compression factor, and the gas can be viewed as an ideal gas when Z is equal to one.

2.1.3. Component transport equations

When multicomponent mass exchange or chemical reactions are involved, the component transport equations need to be solved, which have a differential form [40]:

$$\frac{\partial \rho_m}{\partial t} + \rho_m \nabla \cdot \boldsymbol{U} = \rho D \nabla \cdot \nabla Y_m + \dot{S}_m \tag{6}$$

$$Y_m = \frac{M_m}{M_{tot}} = \frac{\rho_m}{\rho_{tot}} \tag{7}$$

where M_{tot} is the gross mass, g; M_m is the mass of component m, g; ρ_{tot} is the gross density, g/cm^3; ρ_m is the density of component m, g/cm^3; $\dot{S}_m$ is the component source term.

2.2. Physical model

2.2.1. The RNG k-Ɛ turbulence model

When the fuel oil is jetted into the dual-fuel engine, the combustion, complex gas flow, and turbulent combustion phenomena will happen. Throughout this process, the turbulent motion always affects the distribution of various physicochemical reactions and transported substances in the cylinder. Currently, among many turbulence models, the k-Ɛ model has high accuracy and feasibility. Therefore, it is appropriate to use it to simulate the turbulent motion in an internal combustion engine. Its specific equations are as follows [41].

(1) Turbulent energy equation:

$$\frac{\partial \rho k}{\partial t} + \nabla \cdot (\rho k \boldsymbol{U}) = -\frac{2}{3}\rho k \nabla \cdot \boldsymbol{U} + \tau : \nabla \boldsymbol{U} + \nabla \cdot (\alpha_k \mu \nabla k) - \rho \varepsilon + \dot{W}^s \tag{8}$$

(2) Turbulent dissipation equations:

$$\frac{\partial \rho \varepsilon}{\partial t} + \nabla \cdot (\rho \varepsilon \boldsymbol{U}) = -\left(\frac{2}{3}C_1 - C_3 + \frac{2}{3}C_\eta C_\mu \frac{k}{\varepsilon}\nabla \cdot \boldsymbol{U}\right)\rho \varepsilon \nabla \cdot \boldsymbol{U} + \nabla \cdot (\alpha_\varepsilon \mu \nabla \varepsilon) + \frac{\varepsilon}{k}[(C_1 - C_\eta)\tau : \nabla \boldsymbol{U} - C_2 \rho \varepsilon + C_s \dot{W}^s] \tag{9}$$

$$C_3 = \frac{2C_1 - 3m(n-1) + (-1)^\delta \sqrt{6} C_\eta C_\mu \eta - 1}{3} \tag{10}$$

$$C_\eta = \frac{\eta(1 - \eta/\eta_0)}{1 + \beta_k \eta^3} \tag{11}$$

for insulation systems: $m = 0.5$, $n = 1.4$, $\delta = \begin{cases} 1, \nabla \cdot \boldsymbol{U} \le 0 \\ 0, \nabla \cdot \boldsymbol{U} > 0 \end{cases}$; where C_μ is a constant, k is the homogeneous vortex viscosity, cPs/40 °C; $\dot{W}^s$ is the turbulence source term generated by fuel injection, and other relevant parameters reference [41]. The values of the parameters involved are shown in Table 1.

2.2.2. Fuel atomization model

The main models involved in this process are as follows.

(1) Droplet motion model

The velocity of droplet motion can be expressed by the following relation in CONVERGE simulation software [39]:

$$\rho_l V_d \frac{d\boldsymbol{v}_i}{dt} = C_D A_f \frac{\rho_g |\boldsymbol{U}_i|}{2}\boldsymbol{U}_i + \rho_l V_d g \tag{12}$$

$$\boldsymbol{U}_i = \boldsymbol{u}_i + \boldsymbol{u}_i' - \boldsymbol{v}_i \tag{13}$$

where ρ_l is the droplet density, g/cm^3; $\boldsymbol{v}_i$ droplet velocity, m/s; $A_f = \pi r^2$ is the surface area of the liquid droplet front, m^2; g is the acceleration of gravity, m/s^2; ρ_g is the gas density, g/cm^3; C_D is the coefficient of resistance; $\boldsymbol{U}_i$ is the gas-liquid relative velocity, m/s; $\boldsymbol{u}_i$ is the average value of the local velocity, m/s; and $\boldsymbol{u}_i'$ is the turbulent fluctuation gas velocity, m/s.

Table 1
The corresponding parameter values in the above equations [41].

Parameter	C_1	C_1	C_s	β_k	α_k	α_ε
Value	1.42	1.68	1.5	0.012	1.39	1.39

(2) Droplet resistance model

The drag coefficient is divided into static drag coefficient and dynamic drag coefficient [42]. Assuming the droplet is in the case of an ideal sphere, the equations of the coefficient is [43]:

$$C_{\mathrm{d,sphere}} = \begin{cases} 0.424\ ,\ R_{\mathrm{e}} > 1000 \\ \dfrac{24}{R_{\mathrm{e}}}\left(\dfrac{1}{6}R_{\mathrm{e}}^{3/2}+1\right)\ ,\ R_{\mathrm{e}} \le 1000 \end{cases} \tag{14}$$

where R_{e} is the Reynolds number of the droplet.

In practice, when the droplet passes through gas, its shape will be deformed by the influence of gas resistance, at this time, the dynamic resistance coefficient should be considered, and its expression is [43]:

$$C_{\mathrm{D}} = C_{\mathrm{d,sphere}}(2.632y+1) \tag{15}$$

where y is the degree of distortion of the droplet, when $y = 0$, it means that the droplet is not deformed, when $y = 1$, the droplet reaches the extreme deformation situation, at this time the droplet shape is disk-like.

(3) The KH-RT model

The atomization process and oil droplet splitting in combined fuel combustion can be simulated using the KH-RT model [44]. Fig. 1 is the model schematic.

Assumed the nozzle aperture size and the initial droplet diameter size are equal, in the KH model, which is denoted by d_0. Due to the instability of the droplet during its movement, sub-droplets will be separated from the droplet surface, which is denoted by the radius of the sub-droplet in terms of r_{c}, and $r_{\mathrm{c}} = B_0\Lambda_{\mathrm{KH}}$. The main computational equations involved in the KH model are as follows [44]:

$$\Lambda_{\mathrm{KH}} = \frac{9.02r\left(0.4T_{\mathrm{t}}^{0.7}+1\right)\left(0.45\sqrt{Z}+1\right)}{\left(0.865We_{\mathrm{g}}^{1.67}+1\right)^{0.6}} \tag{16}$$

$$\Omega_{\mathrm{KH}} = \frac{0.34+0.38We_{\mathrm{g}}^{1.5}}{(Z+1)\left(1.4T_{\mathrm{t}}^{0.6}+1\right)}\sqrt{\frac{\sigma}{r^3\rho_{\mathrm{g}}}} \tag{17}$$

where r_{c} is the radius of the daughter droplet, μm; Λ_{KH} is the maximum wavelength of the oil beam surface wave, μm; Ω_{KH} is the fastest generation rate for wave generation on the surface of the fuel oil bundle, mm/s; σ is the surface tension, 10^{-3}N/m. We_{g} is the Weber number of the gas. The equations of τ_{KH} and L_{b} are as follows [44]:

$$\tau_{\mathrm{KH}} = \frac{3.726rB_1}{\Omega_{\mathrm{KH}}\Lambda_{\mathrm{KH}}} \tag{18}$$

$$L_{\mathrm{b}} = d_0C_{\mathrm{b}}\sqrt{\frac{\rho_{\mathrm{f}}}{\rho_{\mathrm{g}}}} \tag{19}$$

where τ_{KH} is the droplet breakup time, s; L_{b} is the feature crushing length, μm; B_0 is the model constant determined according to the actual situation, and its size reflects the radius of droplet breakage; B_0 is taken as 0.63 in this study; C_{b} is the constant of the breakage length; ρ_{g} is the density of the gas around the droplet, g/cm^3; ρ_{f} is the density of the droplet, g/cm^3.

Rate of change equation for the liquid drop radius are as follows [44]:

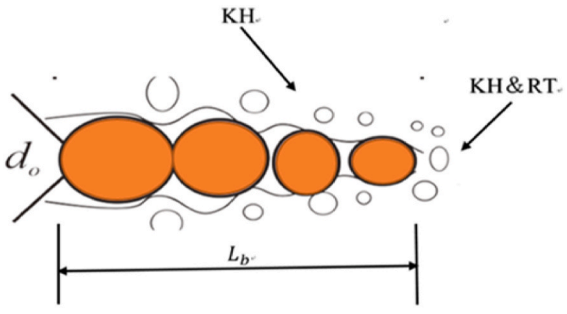

Fig. 1. The KH-RT model.

$$\frac{\mathrm{d}r}{\mathrm{d}t} = -\frac{(r - r_c)}{\tau_{KH}}\ ,\ (r \geq r_c) \tag{20}$$

where r is the radius of the liquid drop before breakage occurs, μm.

In the KH model, the $r_c = \frac{\pi C_{RT}}{K_{RT}}$, where $K_{RT} = \frac{2\pi}{\Lambda_{RT}}$; and the main formulas involved in RT modeling are as follows [44]:

$$\Lambda_{RT} = 2\pi\sqrt{\frac{3\sigma}{-g_t(\rho_f - \rho_g)}} \tag{21}$$

$$\Omega_{RT} = \sqrt{\frac{2\left[-g_t(\rho_f - \rho_g)\right]^{3/2}}{3\sqrt{3\sigma}(\rho_f + \rho_g)}} \tag{22}$$

$$\tau_{RT} = \frac{C_\tau}{\Omega_{RT}} \tag{23}$$

where Z is the Onetzog numeral; T_t is the Taylor numeral; B_1 is the time constant of breakage; K_{RT} is the wavelength that corresponds to the wave with the highest growth rate, μm; Λ_{RT} is the oil beam indicates the maximum wavelength of the generated wave, μm; Ω_{RT} is the wave's quickest creation ratio as measured on the fuel oil bundle's face., mm/s; τ_{RT} is the droplet breakup time, s.

The rate of growth of the unsteady wave in the RT model is solved by considering the viscosity of the gas and the liquid as follow [45]:

$$\omega_{RT} = -K_{RT}^2\left(\frac{\mu_f + \mu_g}{\rho_f + \rho_g}\right) + \sqrt{K_{RT}\left(\frac{\rho_f - \rho_g}{\rho_f + \rho_g}\right)g_t - \frac{\sigma K_{RT}^3}{\rho_f + \rho_g} + K_{RT}^4\left(\frac{\mu_f + \mu_g}{\rho_f + \rho_g}\right)^2} \tag{24}$$

The relational equation for the variation of droplet radius is the same as that in KH, where C_{RT} is other adjustable constants; g_t is the emotional acceleration, mm/s^2; C_τ is a modeling constant, whose value reflects the size of the sub-droplet in the fragmentation process [45]; μ_f is the viscosity of the droplet, g/s·cm^3; and μ_g is the viscosity of the gas around the droplet, g/s·cm^3.

(4) Droplet evaporation model

Upon injecting the oil beam into the cylinder, due to high-temperature reason, the fuel is changed from liquid to gas, resulting in a change in the radius of the droplet. To simulate the droplet evaporation process and determine the change in the droplet's radius, the matching evaporation model must be established. In this study, for the evaporation of the droplet process, the selection of the Frossling relationship [46] for the simulation.

2.2.3. Combustion model

Because of the good applicability of the CFD-coupled chemical reaction kinetics mechanism, it is commonly used to simulate engine in-cylinder combustion. The typical multi-step reaction can be mainly represented by the following relation [40]:

$$\sum_{i=1}^{I} v_{i,r}^{'}\chi_{che,i} \Leftrightarrow \sum_{i=1}^{I} v_{i,r}^{''}\chi_{che,i}\ ,\ r = 1, 2, \ldots, M \tag{25}$$

The net productivity $\dot{\omega}$ of component i is:

$$\dot{\omega} = \sum_{r=1}^{M} v_{i,r}q_r\ ,\ i = 1, 2, \ldots, I \tag{26}$$

The formula for $v_{i,r}$ is:

$$v_{i,r} = v_{i,r}^{''} - v_{i,r}^{'} \tag{27}$$

The progress variable q_r for the rth response is:

$$q_r = k_{fr}\prod_{i=1}^{I}[X_i]^{v_{i,r}^{'}} - k_{rr}\prod_{i=1}^{I}[X_i]^{v_{i,r}^{''}} \tag{28}$$

where I represents the total quantity of the substance; $\chi_{che,i}$ is the chemistry symbol for species i; $v_{i,r}^{'}$, and $v_{i,r}^{''}$ is the stoichiometric values for the components of the reaction and products, respectively, for genus m and reaction r; M indicates the sum of reactions; k_{fr} is the forward rate coefficients for reaction r, and k_{rr} is the reverse rate coefficients for reaction r; $[X_i]$ represents the molar concentration of species i, mol/mL.

2.2.4. Heat transfer models

(1) Cylinder wall heat transfer

The effect of fluid having compressibility is considered in this study. The wall heat transport model that Han and Reitz [47] developed is chosen to calculate the heat transport process at the cylinder wall. The main equations are as follows [47].

The temperature distribution equation is:

$$T_{dis} = 2.1\ln(y_{dim}) + 2.1 S_{dim} y_{dim} + 33.4 S_{dim} + 2.5 \tag{29}$$

The related formula for the wall heat flux is:

$$q_w = \frac{\rho c_p u_{fri} T \ln\left(\frac{T}{T_w}\right) - (2.1 y_{dim} + 33.4)\left(Sv / u_{fri}\right)}{2.1 \ln(y_{dim}) + 2.5} \tag{30}$$

If the source term S could be overlooked in the energy equation, the above equation then becomes:

$$q_w = \frac{\rho c_p u_{fri} T \ln\left(\frac{T}{T_w}\right)}{2.1 \ln(y_{dim}) + 2.5} \tag{31}$$

Where S_{dim} is the dimensionless source term and S_{dim} is given as $S_{dim} = Sv/(q_w u_{fri})$; y_{dim} is the dimensionless extent and y_{dim} is given as $y_{dim} = (y \cdot u_{fri})/v$; y is the distance between the grid and the cylinder wall, m; u_{fri} is the friction velocity, m/s, and u_{fri} is given as $u_{fri} = \sqrt{\frac{\tau_w}{\rho}}$;$v$ is the viscosity of the kinematics, g/(s·cm^3); τ_w is the sheer wall stress, N/m^2; T_w is the cylinder wall temperature, K; T is the cylinder fluid temperature, K; c_p is the constant specific pressure heat capacity, J/(kg·K).

(2) Liquid thermal conduction rate

The liquid thermal conduction rate is calculated as follows [48]:

$$\lambda_l = \frac{X(1 - T_r)^{0.38}}{T_r^{1/6}} \tag{32}$$

$$X = \frac{X^* T_b^{\alpha}}{M^{\beta} T_c^{\gamma}} \tag{33}$$

where λ_l is the liquid thermal conduction rate, W/(m·K); T_r is the lowering of the temperature ratio and $T_r = T/T_{cri}$, T_{cri} is the critical temperature, K. For esters, the values of the parameters in the above equation are shown in Table 2.

2.2.5. Emission model

When biodiesel-hydrogen dual fuels burn in cylinders, the high heat value of hydrogen raises the temperature, so that producing a large amount of NO_x. The generation of NO_x is modeled using the extended Zeldovich mechanism, which contains four chemical components (N, NO, NO_2, N_2O) and nine sets of chemical reaction equations, of which the most prominent reaction equations are listed below [49]:

$$N_2 + O \Leftrightarrow N + NO$$

$$O_2 + N \Leftrightarrow O + NO$$

$$N + OH \Leftrightarrow H + NO$$

When fuel oil burns incompletely in an oxygen-starved engine cylinder, carbon soot is frequently produced. The final soot emission is the difference between the combustion consumption and the amount of generation [50]. In this study, the Kinetic model appendant of CONVERGE software is used to simulate the soot generation, and the control equations of soot emission are as follows [32]:

$$\frac{dM_{sum}}{dt} = \frac{dM_{s,g}}{dt} - \frac{dM_{s,o}}{dt} \tag{34}$$

Table 2
Values of ester-related parameters.

Parameter	X^*	α	β	γ
Value	0.0415	1.2	1.0	0.167

$$\frac{dM_{s,g}}{dt} = A_g M_g p^{0.5} \exp\left(-\frac{E_{s,g}}{RT}\right) \tag{35}$$

$$\frac{dM_{s,o}}{dt} = A_o M_o \left(\frac{p_o}{p}\right) p^{1.8} \exp\left(-\frac{E_{s,o}}{RT}\right) \tag{36}$$

where M_{sum} is the sum of soot, kg; $M_{s,g}$ is the volume of soot generated, kg; $M_{s,o}$ is the volume of soot oxidized, kg; A_g, A_0 are constants; M_g is the amount of fuel evaporated, kg; $E_{s,g}$ denotes the activation energy of the fuel, kJ; M_0 is the amount of oxygen consumed, kg; p_0 is the pressure of the oxygen, Pa; $E_{s,o}$ denotes the activation energy of the oxidization process, kJ; R denotes the gas constant, cal/(K·g·mol).

The chemical kinetic mechanism is very important for the combustion of fuel. In this study, the chemical kinetic mechanism developed by the team was incorporated to precisely imitate the mechanisms of fuel injection and fuel combustion in the previous work [51–53].

2.2.6. Fluid viscosity

The Orrick and Erbar method was used to calculate the fluid viscosity and it can be given as follows [51]:

$$\ln\left(\frac{\eta_L}{\rho_{20} M}\right) = A + \frac{B}{T} \tag{37}$$

where η_L denotes the liquid viscosity, g/(s·cm); ρ_{20} is the density of the liquid at a temperature of 20 °C, g/cm^3; A and B are constants that might be computed using the group contribution technique in documentation [51].

2.2.7. Vapor pressure

For predicting vapor pressure, the Lee-Kesler model is a very successful model, the equation to calculate the vapor pressure are as follows [32]:

$$\ln P_{pv} = f^{(a)}(T_r) + \omega f^{(b)}(T_r) \tag{38}$$

$$f^{(a)}(T_r) = 5.92714 + 0.169347 T_r^6 - 1.28862 \ln T_r - \frac{6.09648}{T_r} \tag{39}$$

$$f^{(b)}(T_r) = 15.2518 + 0.43577 T_r^6 - 13.4721 \ln T_r - \frac{15.6875}{T_r} \tag{40}$$

where P_{pv} denotes the reduced vapor pressure, Pa; and P_{pv} is given as $P_{pv} = P/P_{cri}$; ω is the acentric factor; P_{cri} is the critical pressure, Pa.

2.3. Boundary conditions

A 4190Z diesel engine has been used to power the trials in this research. Detailed information and boundary conditions of the dual-fuel diesel engine used in this study are given in Ref. [32]. Additionally, the amount of cycle injection oil is calculated by the formula [3]:

$$M_x = \frac{\tau_i P_e b_e}{120 n i} \tag{41}$$

where M_x is the cyclic injection volume, g; τ_i is the number of strokes; P_e is the rated power of the engine, kW; b_e is the fuel consumption rate under the rated power, g/kW·h; n is the rotational speed, r/min; i is the number of cylinders.

In addition, the energy fraction of hydrogen is denoted by the symbol HEF in this paper, and the particular formula is as follows [42]:

Table 3
Fuel performance indexes.

Category	Unit	RME	Rapeseed oil	H_2
Lower calorific value	MJ/kg	42.7	39.5	119.8
Cetane number	–	50.0	53.9	8.0
Oxygen content	%	0.3	10.7	–
Latent heat of vaporization	kJ/kg	253.3	273.4	–
Saturation	%	–	4.5	–
Stickiness	cPs/40 °C	2.8	4.6	–
Density at 15 °C	kg/m^3	837.0	882.0	8.5E-2
Flash point	°C	67.0	168.0	−253.0

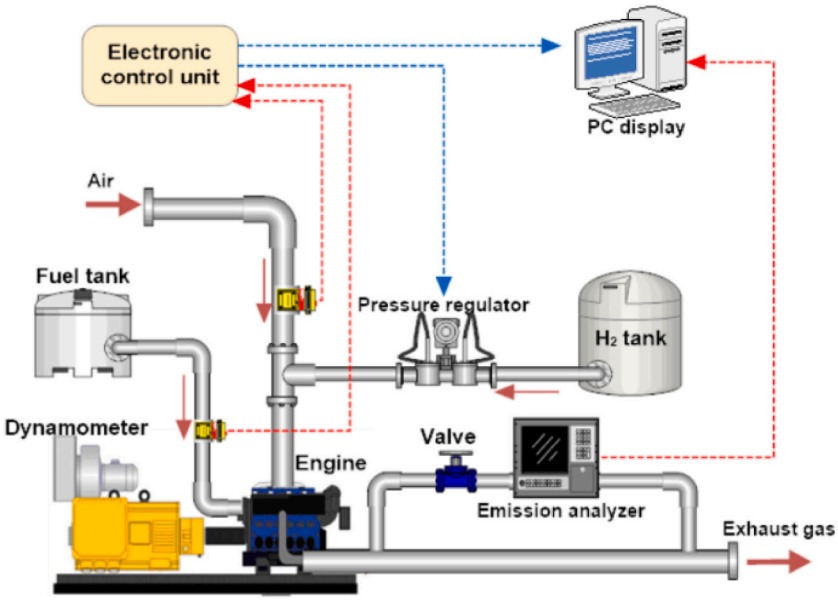

(a)

(b)

Fig. 2. Pictures of the experimental procedure (a) and main experimental setups (b).

$$\mathrm{HEF} = \frac{m_H \cdot Q_H}{m_H \cdot Q_H + m_B \cdot Q_B + m_D \cdot Q_D} \times 100\% \quad (42)$$

where m_H, m_B, and m_D are the mass of H_2, biodiesel, and diesel, g, respectively; Q_H, Q_B, Q_D are the low heating value of H_2, biodiesel, and diesel, kJ/kg, respectively.

The detailed preparation process can be referenced to the earlier work done by our team [3,39,42]. The primary physicochemical characteristics of the fuels utilized in the tests are listed in Table 3 [3,42].

2.4. Experimental procedures

In this study, an experimental four-cylinder, four-stroke, water-cooled diesel engine provided the data needed to confirm the model's dependability. The experimental flow chart and the main experimental setups involved in this study are shown in Fig. 2 (a) and (b), respectively.

For the experiments, an eddy current dynamometer (Xiangyi FC2010) was used to regulate the loads. Exhaust gas concentrations were measured using a Horiba MEXA-1600D/DEGR NO_x pickup meter. The FCMM-2 fuel consumption meter was used to measure the amount of fuel consumed.

To avoid overfilling the engine with hydrogen and causing deflagration, a small amount of hydrogen was blended with biodiesel. The hydrogen system was intended to combine hydrogen and air, which would then be passed via a nozzle, pressure-reducing valve, storage tank, and flow control valve and onto the engine intake manifold. During the testing process, the sensors' varied signals are transformed into voltage signals before being sent to the emission and combustion analyzers. The following are the equivalent experimental steps.

Step 1. Get ready before firing up the diesel engine.

(1) : Preparing the biodiesel and characterizing its chemical and physical qualities based on the international identification mark.
(2) : Examine the emission monitoring system, cooling water system, and lubricating oil system of the diesel engine.

Step 2. Engine test.

(1) : Starting the diesel engine, load control equipment, and testing equipments.
(2) : Adjustment of loads. The experiments were conducted by a marine diesel engine under three various load conditions (50 %, 75 %, and 100 %). After 20 minutes, the engine operation was stabilized, and the experimental findings were recorded. The three separate experimental data were recorded and averaged to ensure steady-state measurements.

Step 3. Analyze and process experimental results.

2.5. Uncertainty analysis

In the actual work, a certain degree of uncertainty will be produced due to observation, sensors, and other objective factors. So, to carry out the uncertainty analysis is indispensable [53]. Table 4 shows the scale and precision of the measurement instruments corresponding to each parameter used in the experiment, and for the total experimental uncertainty, its calculation formula is as follows [42]:

$$Q_r = \left\{ [u_1(\partial R/\partial Z_1)]^2 + [u_2(\partial R/\partial Z_2)]^2 + \cdots + [u_n(\partial R/\partial Z_n)]^2 \right\}^{1/2}, \; R = (Z_1, Z_2, \ldots, Z_n) \quad (43)$$

where u_1, u_2, …, u_n are the uncertainty of the results; Z_1, Z_2, …,Z_n are independent covariate of each uncertainty.

Table 4
Inconsistency of associated parameters.

Parameters	Measurement range	Accuracy	Indeterminacy (%)
NO_x emission	0–5000 ppm	±10 ppm	±0.50
CO_2 emission	0–16 % vol	±0.46 %	±1.00
HC emission	0–15000 ppm	±10 ppm	±11.0
CO emission	0–10 % vol	±0.3 %	±0.30
Pressure	0–25 MPa	±10 KPa	±0.50
Exhaust gas temperature	0–1000 °C	±1 °C	±0.25
BSFC	–	–	±1.50
Engine speed	1–2000 rpm	±0.2 %	±0.24
Crank angle encoder	0-720°CA	±0.125°	±0.30

2.6. Mesh selection

In this study, a corresponding dynamic mesh was developed based on the geometry of a dual-fuel engine, and a piston type with an eighth of the diameter and a 150° injection cone angle was developed. In the modeling process, a proper selection of the mesh is necessary. The cylinder pressure at 75 % load for three distinct mesh sizes is displayed in Fig. 3. It can be found that a mesh division of 2.0 mm size is the most appropriate to be chosen for the simulation.

2.7. Model validation

To validate the CFD model, Fig. 4 compares the experimental and simulation results of dual-fuel engine combustion with 5 % hydrogen addition. The figure shows that the cylinder pressures obtained from the simulation are lower than the experimental results by about 0.08 MPa, −0.15 MPa, and −0.20 MPa. The errors between the experimental and simulation data of the exergy rate at different loads are within the acceptable range.

Fig. 5 compares simulated and experimental data for NO_x and HC emissions at various loads. The maximum errors are all within 5 %. Therefore, the dual-fuel engine's combustion and exhaust characteristics can be simulated by the established CFD model.

3. Results and discussion

The influence of EGRs on the biodiesel-hydrogen dual-fuel engine is examined and analyzed under four distinct load circumstances, based on the constructed 3D CFD model.

3.1. In-cylinder pressure

Fig. 6 shows the impact of various EGR rates on the in-cylinder pressure at different loads. Under 50 % load, the highest in-cylinder pressures for 5 %, 10 %, and 15 % EGR rates were reduced by 2.96 %, 6.41 %, and 18.74 %, respectively compared with the highest in-cylinder pressure under 0 % EGR rate. When the EGR rate rises, it leads to a lower fresh air content, and the oxygen content is less relatively. Furthermore, with increasing load comes an increase in in-cylinder pressure. For instance, under 75 % load, the highest in-cylinder pressure at 5 %, 10 %, and 15 % EGR rates decreased by 2.72 %, 5.88 %, and 12.28 %, respectively, from the highest in-cylinder pressure at 5 % EGR rate. However, as EGR increases, the oxygen decreases, then further worsening combustion.

3.2. In-cylinder temperature

Fig. 7 illustrates the impact of various EGR rates on the in-cylinder temperature under distinct loads at a hydrogen addition rate of 10 % in biodiesel. The lowering of the peak in-cylinder temperature is more noticeable the greater the EGR rate. For instance, under 50 % load, the in-cylinder temperature is at its maximum when the EGR rate is 0 %. Compared with the cylinder temperatures at 0 % EGR, the peak in-cylinder temperatures with EGR rates of 5 %, 10 %, and 15 % are reduced by 1.27 %, 5.39 %, and 17.49 %, respectively. Thus, the suitable EGR rate can lower the in-cylinder temperature and further reduce the content of NO_x.

Table 5 is the cloud maps of the in-cylinder temperature field for three distinct loads with different EGR rates at a crankshaft rotation angle of 10°CA. These cloud maps demonstrate how the engine cylinder's localized high-temperature zone shrinks as the EGR rate rises. Thus, the EGR can increase the cylinder temperature.

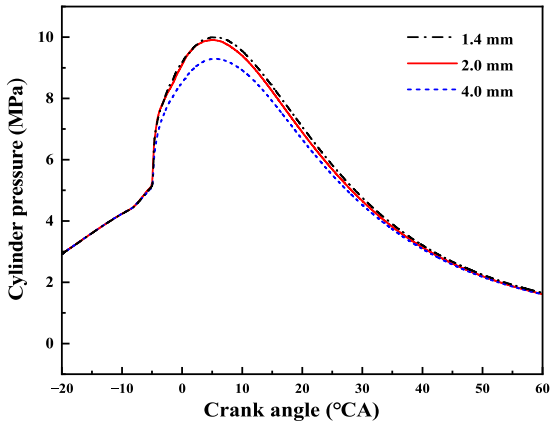

Fig. 3. In-cylinder pressures at 75 % load for various grid sizes.

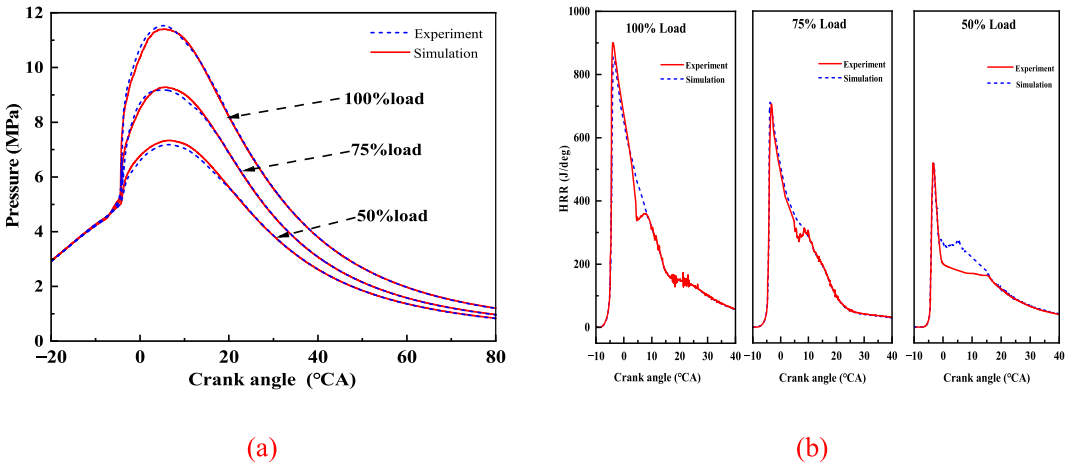

Fig. 4. Graphs of comparative results for blended fuels with 5 % hydrogen content. (a) Comparison of internal cylinder pressures; (b) Comparison of HRR.

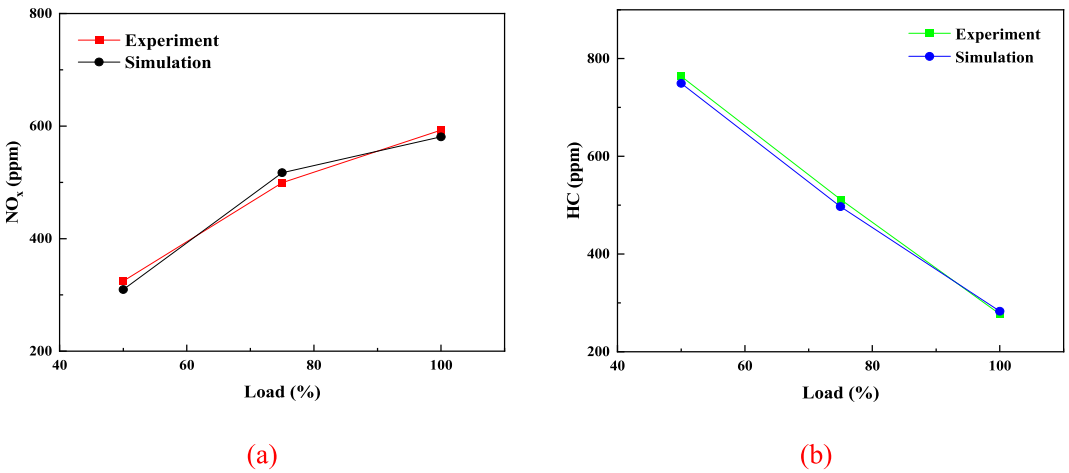

Fig. 5. Graphs of comparative results for emissions under various loads. (a) Comparison of NO_x emission; (b) Comparison of HC emission.

3.3. BSFC

Fig. 8 illustrates the impact of various EGR rates on the BSFC under distinct loads at a hydrogen addition rate of 10 % in biodiesel. For example, when the EGR rates are 0 %, 5 %, 10 %, and 15 % at 50 % load, the BSFCs are 370.72g/(kW·h), 376.23 g/(kW·h), 378.97 g/(kW·h), and 381.87 g/(kW·h), respectively. Moreover, in comparison with BSFC at 0 % EGR, BSFCs of 5 %, 10 %, and 15 % are increased by 1.49 %, 2.23 %, and 3.01 %, respectively. As the EGR rate rises, the volume of exhaust gas in the cylinder rises, which reduces the oxygen level in the cylinder, resulting in a larger localized anoxic region. It inhibits the fuel oil in the cylinder from oxidizing, which results in inadequate fuel oil combustion, thus increasing the engine fuel consumption [53].

3.4. Brake thermal efficiency

Fig. 9 shows the effect of various EGR rates on thermal efficiency under distinct loads at a hydrogen addition rate of 10 % in biodiesel. For example, compared with BTE at EGR = 0 %, as the EGR rate increases to 5 %, 10 %, and 15 % under 75 % load, the BTEs are decreased by 2.42 %, 3.56 %, and 4.68 %, respectively. The rise in exhaust gas in the intake air relatively decreases the in-cylinder oxygen level, which is detrimental to the perfect combustion of the fuel oil, and consequently lowers the engine's thermal efficiency [54].

3.5. Soot emission

Fig. 10 (a), (b), and (c) demonstrate the impact of various EGR rates on soot emission under distinct loads at a hydrogen addition

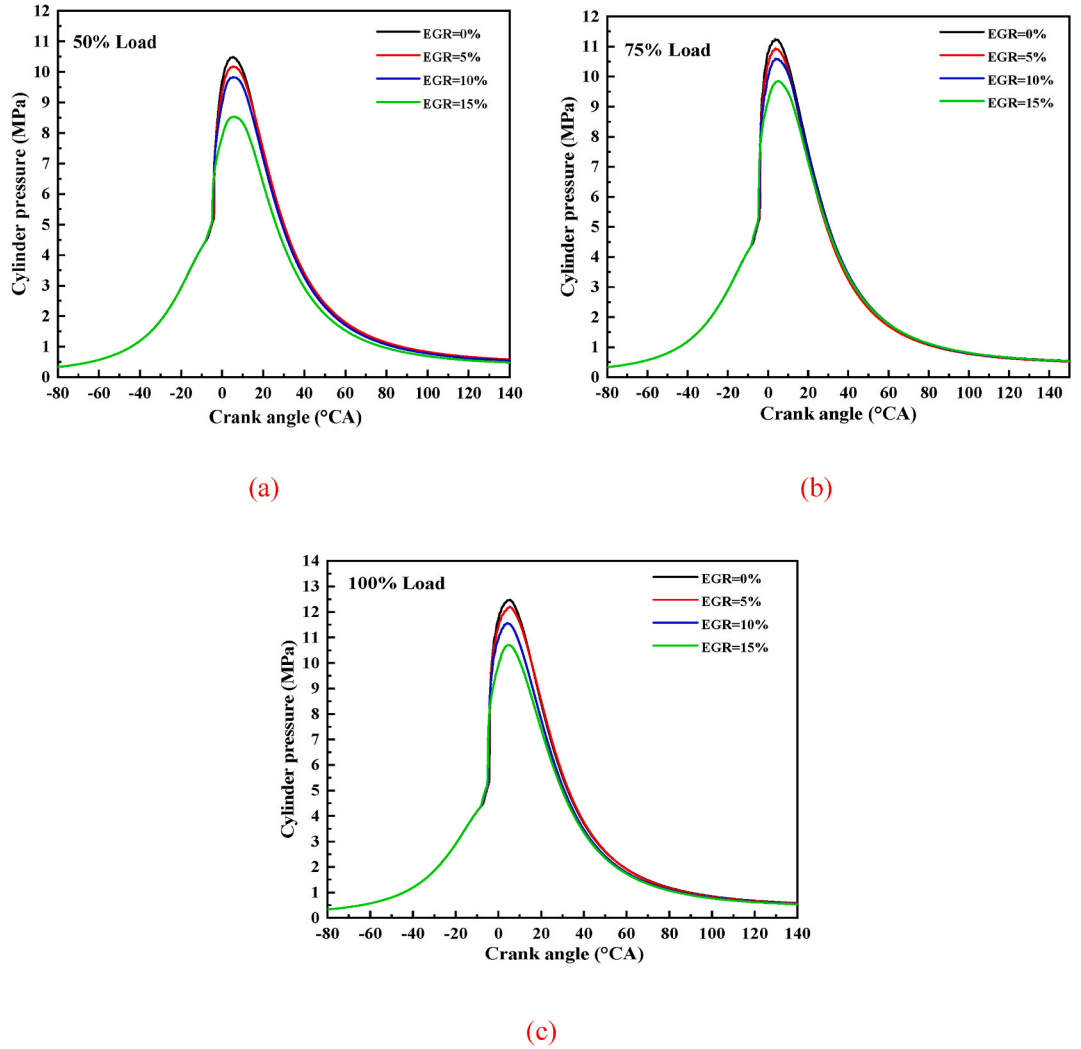

Fig. 6. The impact of various EGR rates on the in-cylinder pressure under distinct loads at a hydrogen addition rate of 10 % in biodiesel. (a) Under 50 % load; (b) Under 75 % load; (c) Under 100 % load.

rate of 10 % in biodiesel. Fig (d) shows the soot content for three different load conditions and different EGR rates. It is evident that as the EGR rate rises, soot content rises as well. This is because that as the EGR rate increases, it inhibits the oxidation of carbon soot, leading to a rise in the formation of soot precursors. Thus causing an increase in soot emission [55].

3.6. CO emission

In Fig. 11, (a), (b), and (c) show the plots of CO emission with crankshaft angle for different EGR rates at specific load conditions, respectively. Fig (d) shows the CO content for three different load conditions and different EGR rates. These plots show that, under all three loads, CO emission rose as the EGR rate increased, with the effect of an increase in CO emission becoming more noticeable as the EGR rate grew. The cause of this result is that as the EGR rate rises, there is a relative decrease in the amount of oxygen entering the cylinders, preventing the fuel from combusting adequately. As a result, more CO is produced.

3.7. HC emission

In Fig. 12, (a), (b), and (c) show the plots of HC emission with crankshaft angle for different EGR rates at specific load conditions, respectively. Fig (d) shows the HC content for three different load conditions and different EGR rates. These plots demonstrate how, under the three loads, the HC emission rose as the EGR rate increased. This is because the cylinder's oxygen concentration drops as the EGR rate rises. There is insufficient fuel burnt during combustion and a higher likelihood of the flame going out close to the cylinder walls. Thus, the HC emission increases.

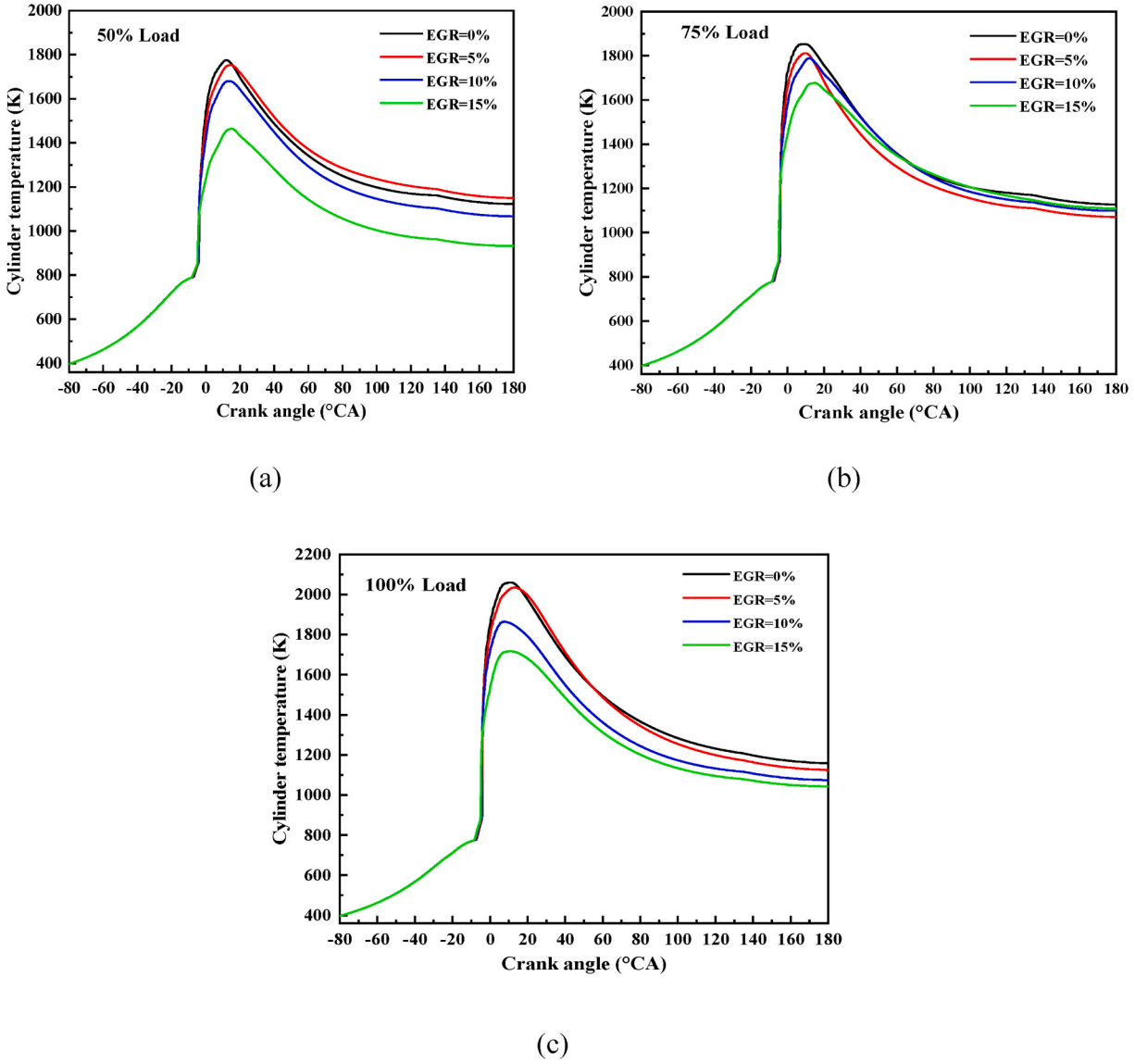

Fig. 7. The impact of various EGR rates on the in-cylinder temperature under distinct loads at a hydrogen addition rate of 10 % in biodiesel. (a) Under 50 % load; (b) Under 75 % load; (c) Under 100 % load.

3.8. NO_x emission

In Fig. 13, (a), (b), and (c) shows the plots of NO_x emission with crankshaft angle for different EGR rates at specific load conditions, respectively. Fig (d) shows the NO_x content for three different load conditions and different EGR rates. These figures show that when the EGR rate increased, the NO_x emission under the three loads reduced. This is because a rise in the EGR rate increases the volume of exhaust gases, which reduces the average temperature in the cylinder. As the temperature in the engine decreases, it reduces the activation energy of the reaction that produces NO_x. Besides, when the EGR rate increases, exhaust gas is introduced, which comparatively lowers the amount of oxygen available for burning [56]. Thus, the lower NO_x emission has occurred.

Table 6 shows the NO_x distribution of the cylinder at four different EGR rates at three distinct loads at a hydrogen addition rate of 10 % in biodiesel. These cloud maps show the NO_x distribution in the engine cylinder, which indicates a decreasing trend of NO_x content as a rise in the EGR rate. Combined with the cloud plot of in-cylinder combustion temperature distribution in Table 5. These cloud maps indicate that NO_x is mainly distributed in the region of higher temperature. This is mainly because NO_x production is largely affected by temperature, and the in-cylinder temperature drops as the EGR rate increases, which is unfavorable to the generation of NO_x. This leads to a lower NO_x emission.

Table 5
Cloud maps of in-cylinder temperature field with different EGR rates under three different load conditions at 10°CA.

	50% Load	75% Load	100% Load
EGR=0%	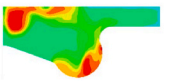	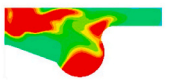	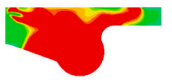
EGR=5%	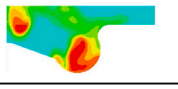	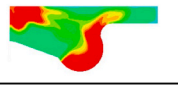	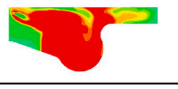
EGR=10%	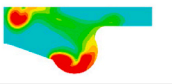	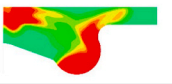	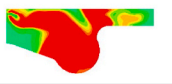
EGR=15%	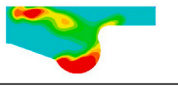	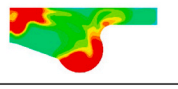	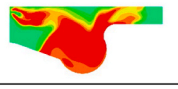
Temperature (K): 500 640 780 920 1060 1200 1340 1480 1620 1760 1900			

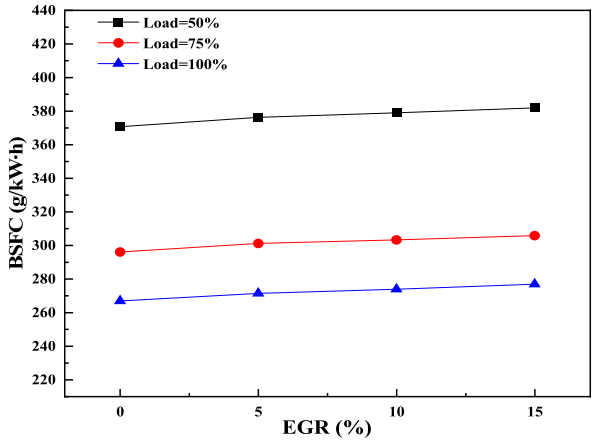

Fig. 8. The impact of various EGR rates on the BSFC under distinct loads at a hydrogen addition rate of 10 % in biodiesel.

4. Multi-objective optimization

In this section, the effects of hydrogen mixing ratios (0 %, 5 %, 10 %, and 15 %), loads (50 %, 75 %, and 100 %), and EGR ratios (0 %, 5 %, 10 %, and 15 %) on the BSFC, NO_x emission, and HC emission of the dual-fuel engine are investigated. Optimization was carried out using RSM to obtain the best BSFC, along with the lowest NO_x emission and HC emission values. RSM was originally proposed by Box and Wilso in 1951. Later, Montgomery and Myers redefined the RSM by combining statistics and mathematics in engineering optimization, so that it could be applied to more fields and analyze the interlocking effects of corresponding factors on the experimental results [57].

4.1. Experimental design and modeling

In this study, RSM is applied to establish a response surface model for a dual-fuel engine, which is used to predict the BSFC, NO_x emission, and HC emission. Then the experimental variables and the response data are fitted by regression equations to obtain the corresponding functional relationships, and finally, the optimal solutions are derived by analyzing them. The pertinent set parameters were created using the Box-Behnken design of experiments methodology. It involved three different parameter ranges: 0 %–15 % for the hydrogen fraction, 50 %–100 % for the load, and 0 %–15 % for the EGR rate. The quadratic model equations for RSM are as follows [32]:

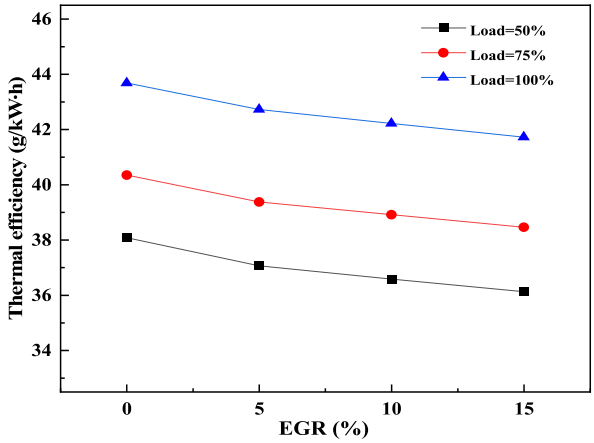

Fig. 9. The impact of various EGR rates on thermal efficiency under distinct loads at a hydrogen addition rate of 10 % in biodiesel.

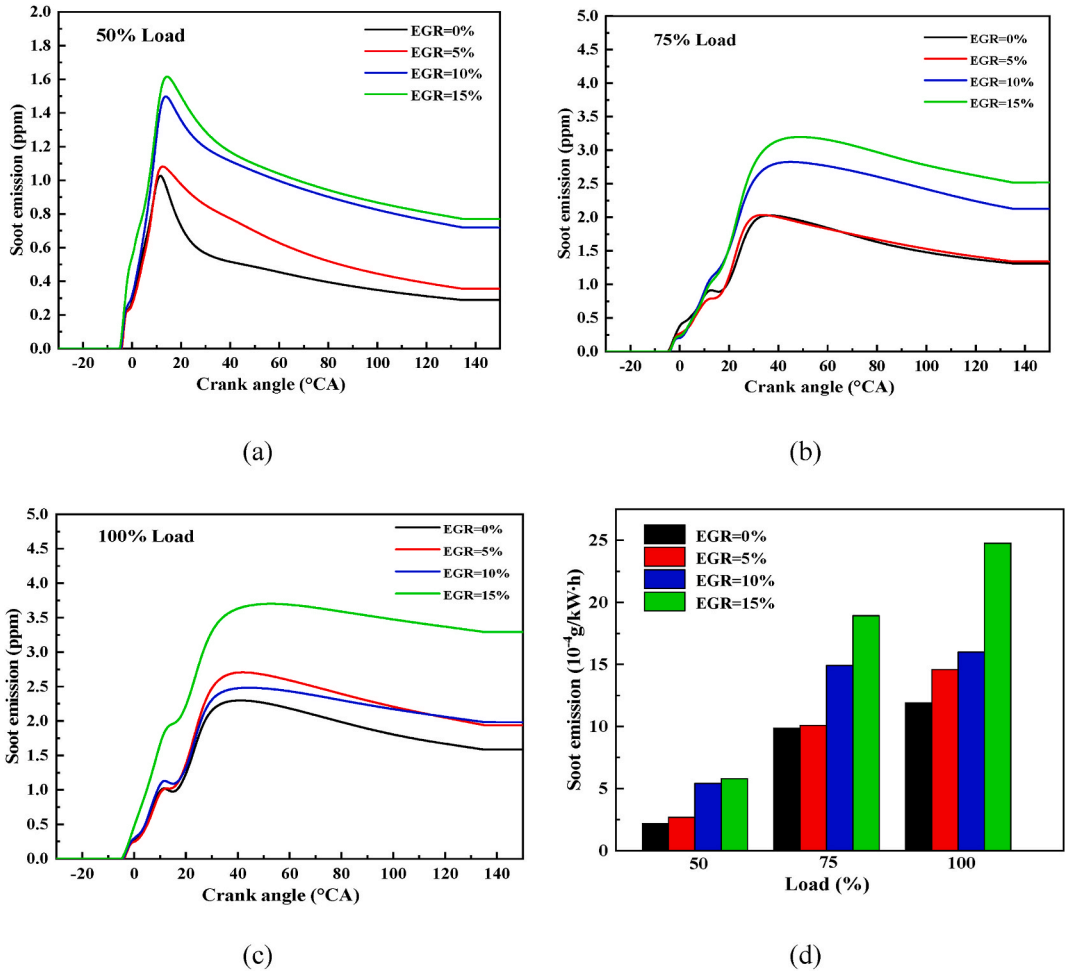

Fig. 10. The impact of various EGR rates on soot emission under distinct loads at a hydrogen addition rate of 10 % in biodiesel.

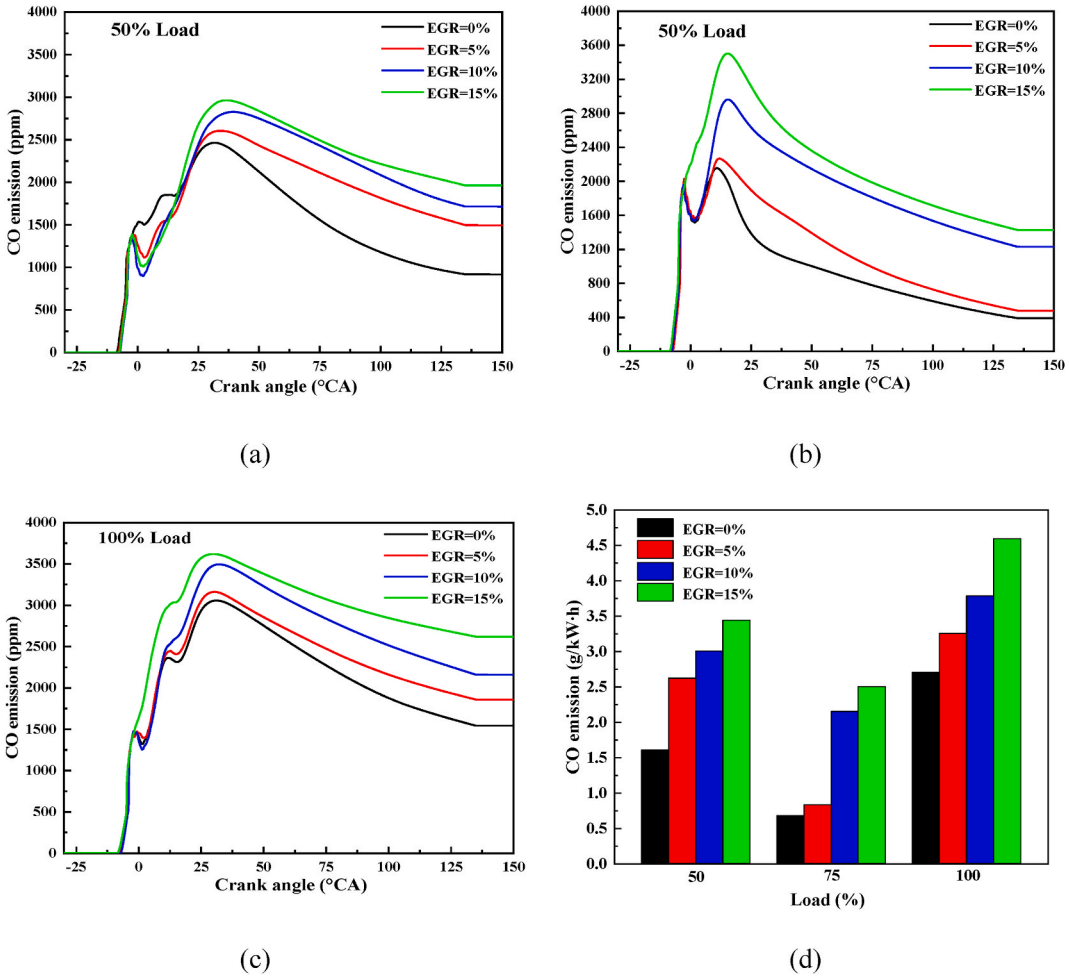

Fig. 11. The impact of various EGR rates on CO emission under distinct loads at a hydrogen addition rate of 10 % in biodiesel.

$$K = N_0 + \sum_{i=0}^{I} M_i N_i + \sum M^2 N_{ii} + \sum_{i<j=2} M_i M_j N_{ij} \tag{44}$$

$$K = \left(M^T M\right)^{-1} M^T Z \tag{45}$$

where N_0 is a parameter constant; N_i is the parameter that includes all linear terms; N_{ii} is the parameter of the quadratic term; N_{ij} is the parameter of the interaction term; M is the calculation matrix; M^T is the required characteristic matrix and is the transposition of M and Z.

The accuracy can be calculated by Ref. [32]:

$$\Theta = \frac{100}{n} \sum_{i=0}^{n} \left| \frac{z_{i,\mathrm{ecpt}} - z_{i,\mathrm{pred}}}{z_{i,\mathrm{pred}}} \right| \tag{46}$$

where n is the test number; $z_{i,ecpt}$ is the measurement value of the homologous test; $z_{i,pred}$ is the predicted value homologous to the test.

The response variables for BSFC, NO_x emission, and HC emission were fitted by using the least squares method, and the results were obtained using CONVERGE software in combination with the above simulation model. The following are the regression equations for BSFC, NO_x emission, and HC emission (from software):

$$BSFC = 327.06 - 41.59x - 47.46y + 22.82z - 0.6413xy - 8.81xz + 5.12yz - 5.81x^2 + 5.19y^2 + 15.49z^2 \tag{47}$$

$$NO_x = 400 + 138.3x + 119.12y - 72.11z + 45.92xy - 13.29xz - 24.18yz + 17.97x^2 - 10.86y^2 + 15.42z^2 \tag{48}$$

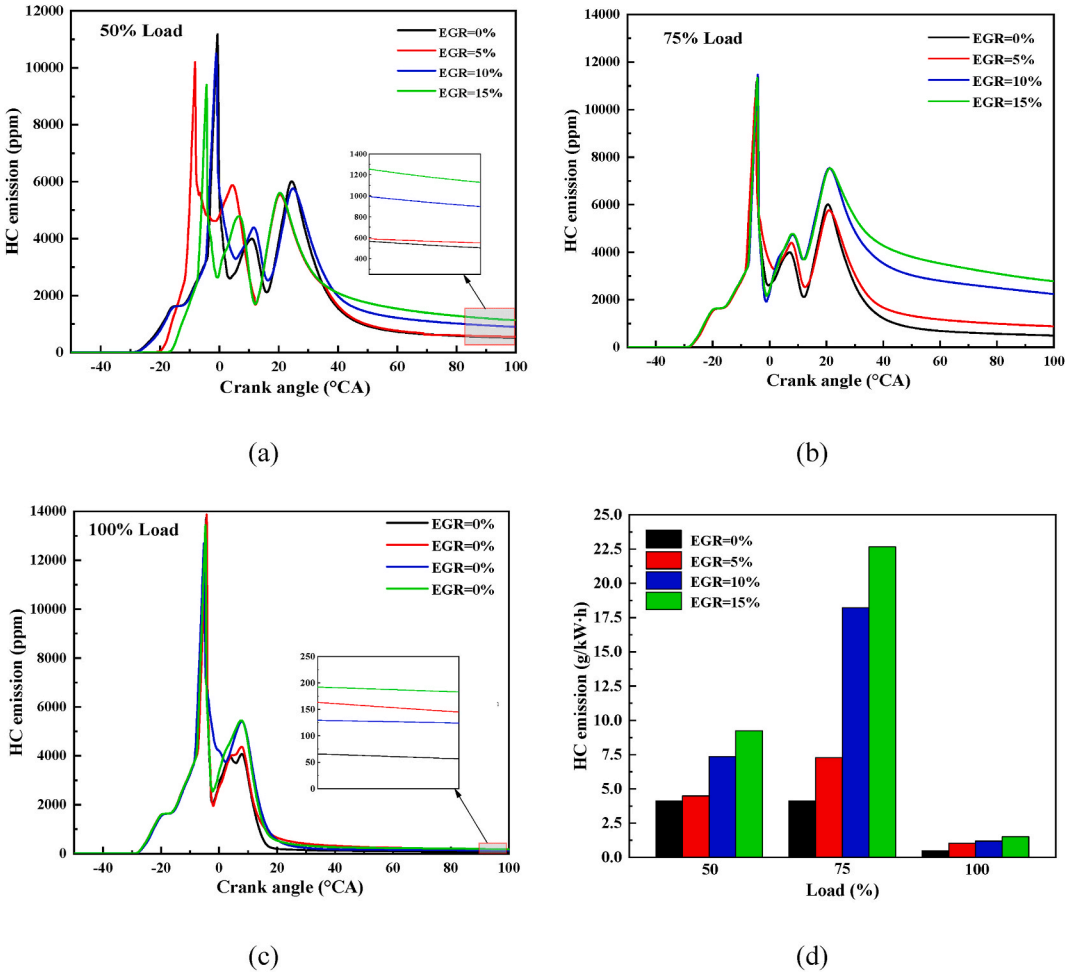

Fig. 12. The impact of various EGR rates on HC emission under distinct loads at a hydrogen addition rate of 10 % in biodiesel.

$$HC = 563.2 - 115.45x - 237.62y + 32z - 12.47xy + 35.52xz + 29.81yz - 45.78x^2 + 2.16y^2 - 25.62z^2 \quad (49)$$

where x is the hydrogen percentage, %; y is the load percentage, %; z is the EGR percentage, %.

Table 7 displays the ANOVA parameters for the BSFC, NO_x, and HC emissions. It can be seen that the P-value is less than 0.0001, which means that the model is reasonable. In addition to this, the fit (R^2), prediction (Pre-R^2), and adjustment (Adj-R^2) of the response are all greater than 0.93. So the RSM has great accuracy in predicting and reliability of the experimental outcomes because the distinction among Pred-R^2 and Adj-R^2 is smaller than 0.1.

The contrast of the predicted and actual values is shown in Fig. 14. The residual difference is the distinction between the actual and projected values. The engine's BSFC, NO_x emission, and HC emission all fall within the desirable range, as can be seen from the extremely little variation between anticipated and experimental data. The predicted values are in a positive proportional function relationship with the actual values, and the confidence level of all the responses to the regression model in the figure is more than 95 %, which indicates a good fit of the model developed. So it can more accurately predict the BSFC, NO_x emission, and HC emission of the dual-fuel engine.

4.2. Optimization for BSFC

Fig. 15 shows the impact of three variables on BSFC. In the figure, the effect of each variable on the target is reflected by the trend of the corresponding curve. The larger values of the variables corresponding to the F values in Table 8 indicate a greater influence on the BSFC. Therefore, the order of the degree of influence on BSFC is load > hydrogen fraction > EGR rate. In this case, the relationship between load and hydrogen fraction on BSFC is a negative correlation. As the load and hydrogen fraction increase, the flame propagation rate of the fuel mixture is accelerated, which in turn improves the in-cylinder burning process of the engine and reduces the BSFC. The influence of the EGR rate on the BSFC starts with a slow effect at the beginning, and then the BSFC rises dramatically due to

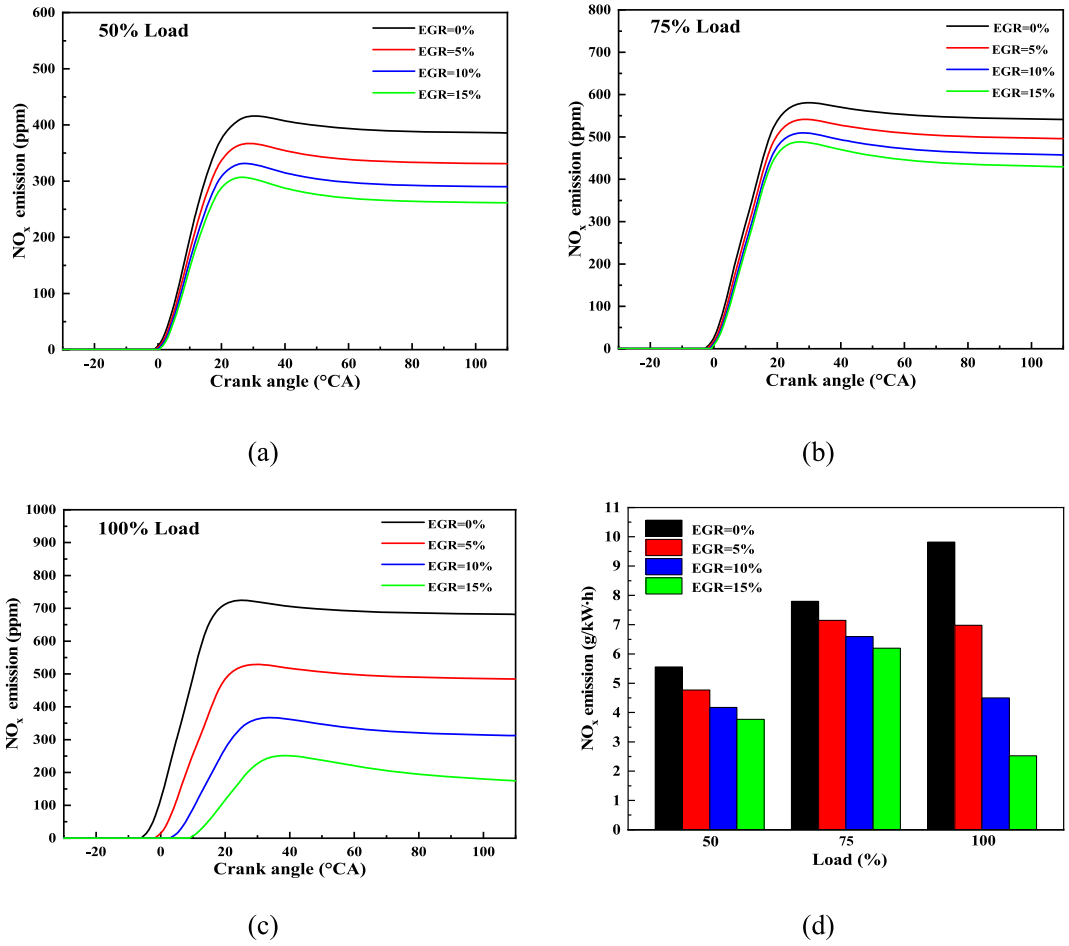

Fig. 13. The impact of various EGR rates on NO_x emission under distinct loads at a hydrogen addition rate of 10 % in biodiesel.

Table 6
Cloud maps of NO_x in the cylinder with different EGR rates under three different load conditions at 10°CA.

	50% Load	75% Load	100% Load
EGR=0%	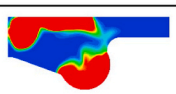	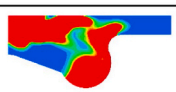	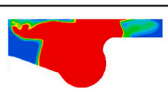
EGR=5%	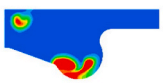	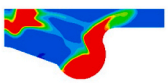	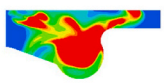
EGR=10%	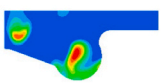	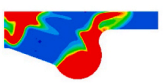	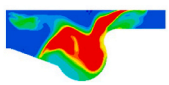
EGR=15%	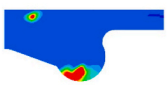	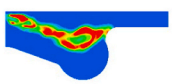	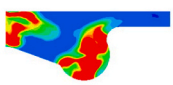
NOx (ppm):	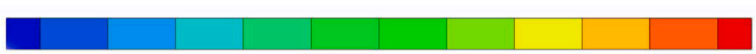 0 25 50 75 100 125 150 175 200 225 250		

Table 7
ANOVA table of HC, NO_x, and BSFC.

Source	HC model		NO_x model		BSFC model	
	F-value	P-value (10^{-4})	F-value	P-value (10^{-4})	F-value	P-value (10^{-4})
Model	188.81	<1	536.42	<1	162.96	<1
x	284.46	<1	2224.9	<1	465.32	<1
y	1250.22	<1	1715.83	<1	627.51	<1
z	24.94	5	689.16	<1	158.89	<1
xy	2.17	1819	152.72	<1	0.0683	7987
xz	17.26	21	13.15	48	13.25	45
yx	11.85	65	42.53	<1	4.36	638
x^2	14.79	31	12.41	55	2.98	1150
y^2	0.0364	8525	5.56	405	2.96	1175
z^2	4.56	588	8.86	133	20.91	10
R^2 (10^{-4})	9945		9978		9933	
Adj-R^2 (10^{-4})	9885		9960		9874	
Pred-R^2 (10^{-4})	9024		9662		9410	

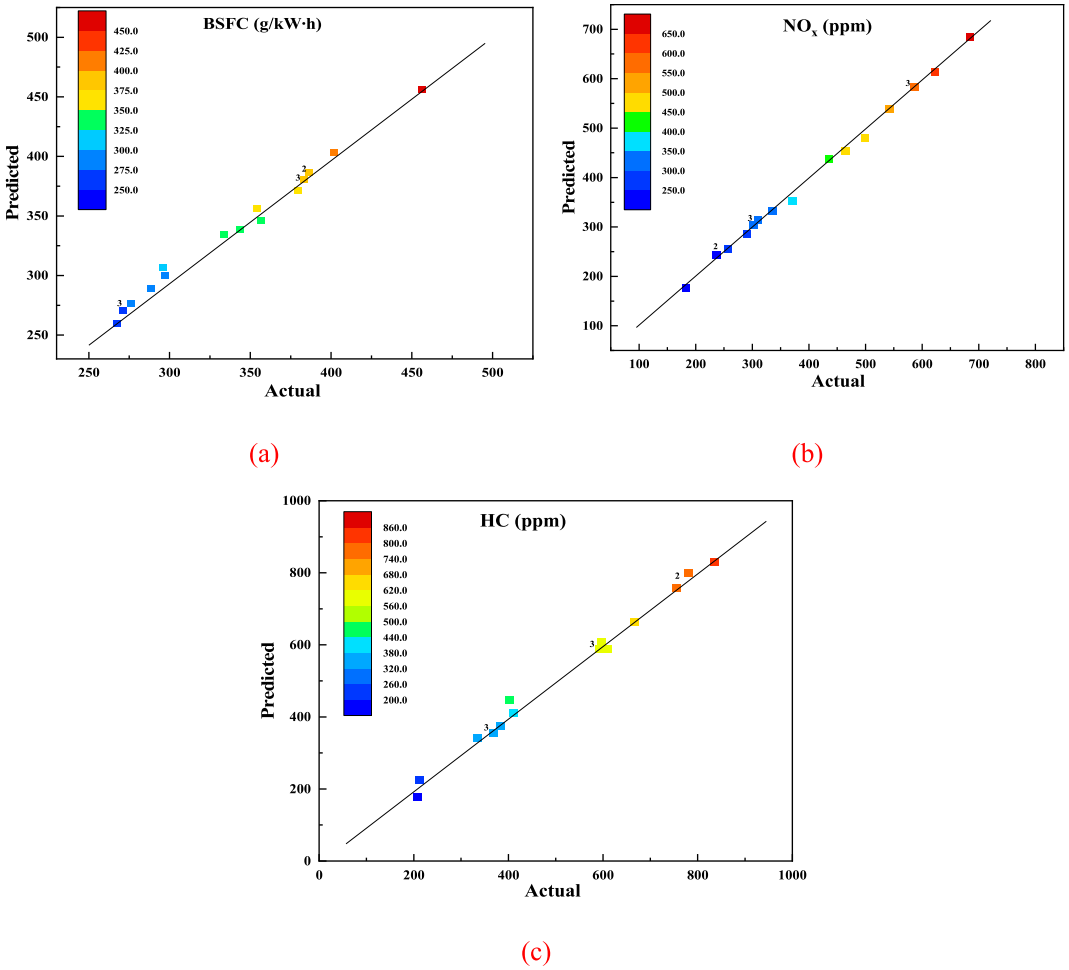

Fig. 14. Comparisons of predicted and actual parameters. (a) BSFC comparison graph; (b) NO_x emission comparison graph; (c) HC emission comparison graph.

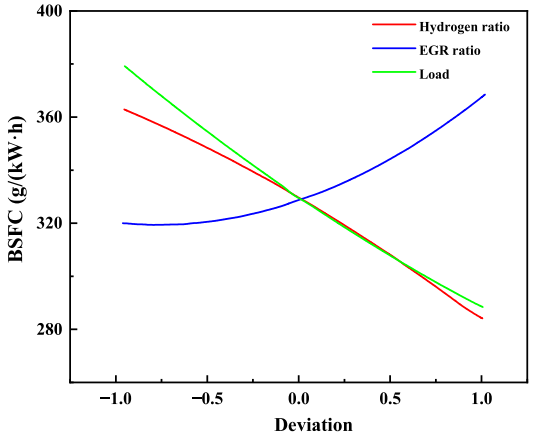

Fig. 15. The impact of three variables on BSFC.

Table 8
Contrast of experimental verification and prediction.

H_2 (%)	Load (%)	EGR (%)		BSFC (g/kW • h)	NO_x (g/kW • h)	HC (g/kW • h)
			Actual	290.43	6.7415	2.801
6.92	100	7.68	Predicted	288.24	6.9865	2.736
			Error(%)	−0.75	3.63	−2.33

the rise of the EGR rate. This is caused by increased EGR rates, which lower the oxygen content of the engine cylinder. Thus, poor combustion increases the BSFC.

Graphs (a), (b), and (c) in Fig. 16 are the surface graphs of the effects of two different variables on BSFC, respectively. These graphs demonstrate the EGR rate is positively correlated with the BSFC and the BSFC reaches the maximum at EGR = 15 %. In addition, higher loads and hydrogen fractions will reduce the BSFC.

4.3. Optimization for NO_x emission

Fig. 17 shows the order of the influence degree on NO_x emission: EGR rate > hydrogen fraction > load. It is mostly because the amount of fresh air and oxygen percentage entering the cylinder falls as the EGR rate is increased. Then, the speed of flame traveling is reduced and the temperature increase rate is also reduced. Furthermore, large load and high hydrogen percentage raise the cylinder's temperature, which facilitates the interaction of nitrogen and oxygen. Large amounts of NO_x pollutants are produced as a result.

Graphs (a), (b), and (c) in Fig. 18 are the surface graphs of the effects of two different variables on NO_x emission, respectively. These graphs demonstrate that load and hydrogen percentage have a great effect on the increase in NO_x emission. Furthermore, the rise of the EGR rate signally reduces the NO_x emission. Therefore, the introduction of an appropriate EGR rate at high load and high hydrogen percentage results in optimum NO_x emission.

4.4. Optimization for HC emission

Table 7 demonstrates the highly significant (p0.0001) connection among the hydrogen percentage, engine load, and EGR rate on HC emission. R^2, Adj-R^2, and Pred-R^2 on HC had values of 99.42 %, 98.89 %, and 90.23%, respectively. So, the model is well suited for predicting HC emission.

Fig. 19 shows the diverse plots of the effects of three different variables on HC emission. The figure shows that the order of magnitude affecting HC emission is: load factor > hydrogen ratio > EGR rate, with load factor having the most significant effect on HC emission. As the load increases, the HC emission decreases significantly, especially at 100 % load. When the hydrogen percentage rises from 0 % to 15 %, the decrease of HC emission reaches 39.7 %, which is because the rise of hydrogen leads to the rise of H and OH radical concentration in the engine cylinder.

Graphs (a), (b), and (c) in Fig. 20 are the surface graphs of the effects of two different variables on HC emission, respectively. These graphs show that the HC emission emerges a small increase with increasing EGR rate. In addition, a larger load and higher hydrogen percentage favor the reduction of HC emission.

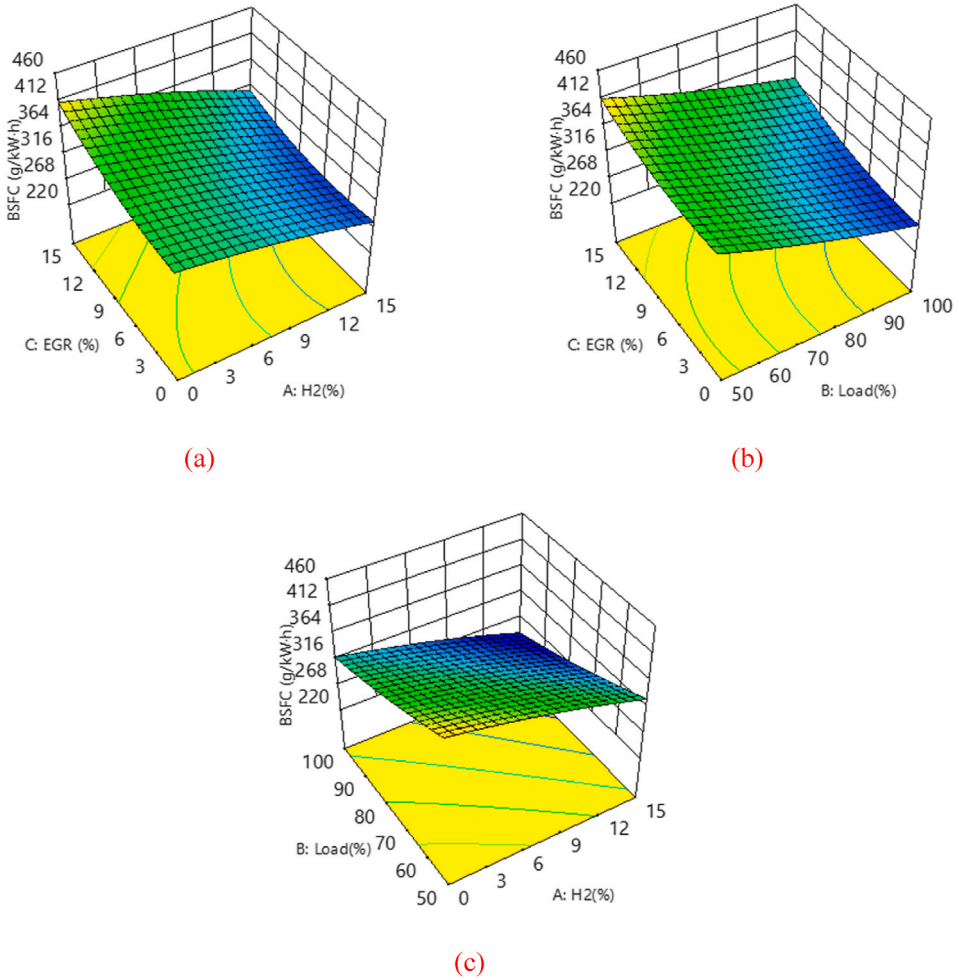

Fig. 16. Surface graphs of the effects of different variables on BSFC. (a) Different EGR rates and H_2 contents on BSFC; (b) Different EGR rates and load rates on BSFC; (c) Different load rates and H_2 contents on BSFC.

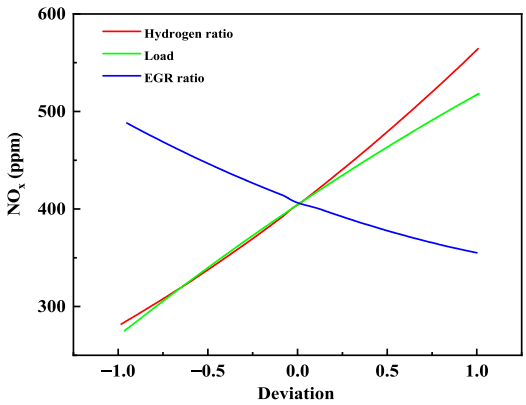

Fig. 17. The impact of three variables on NO_x emission.

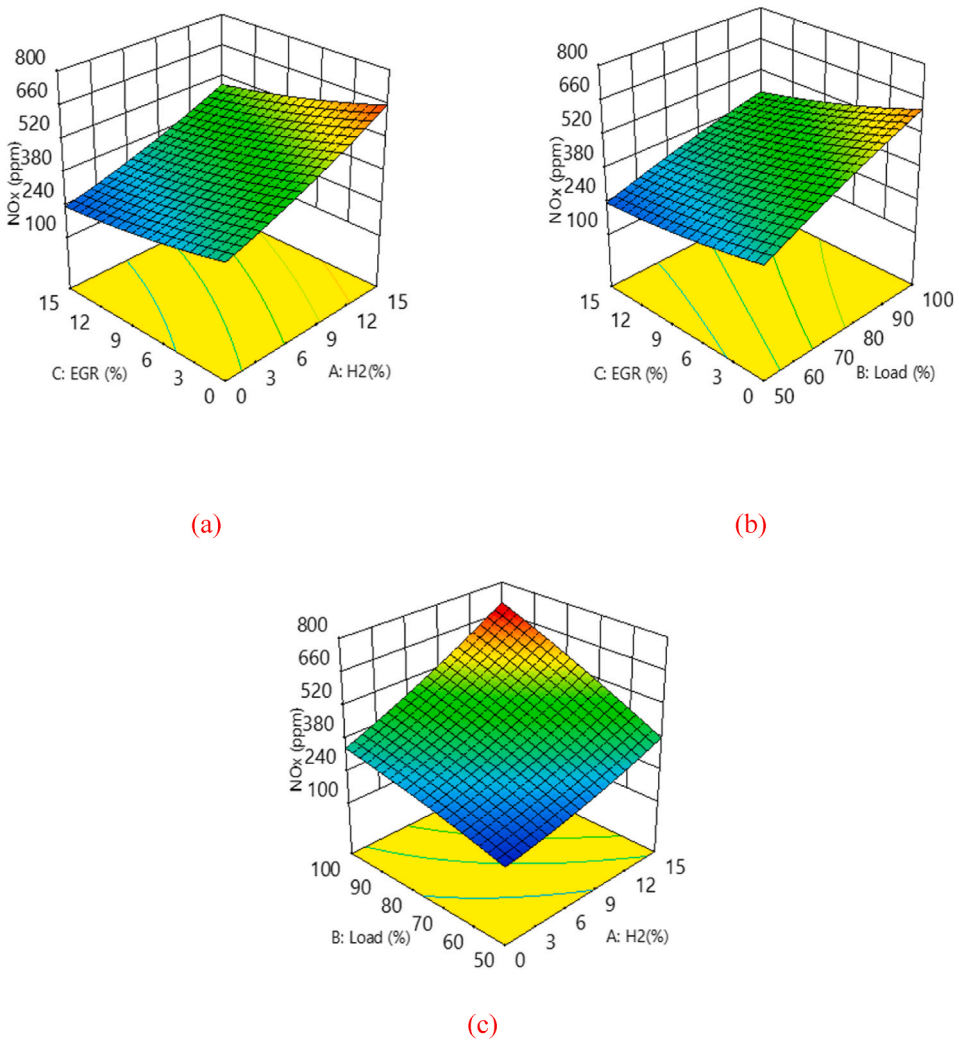

Fig. 18. Surface graphs of the effects of different variables on NO_x emission. (a) Different EGR rates and H_2 contents on NO_x; (b) Different EGR rates and load rates on NO_x; (c) Different load rates and H_2 contents on NO_x.

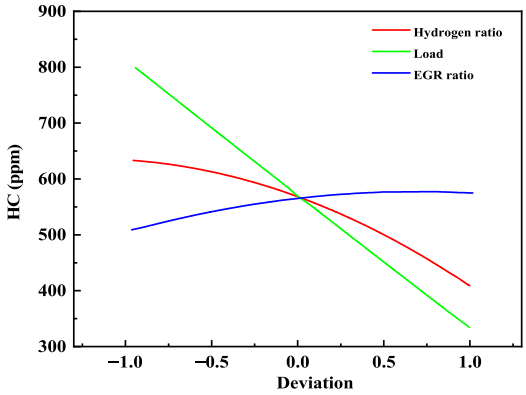

Fig. 19. Disturbance results of the impact of different variables on HC emission.

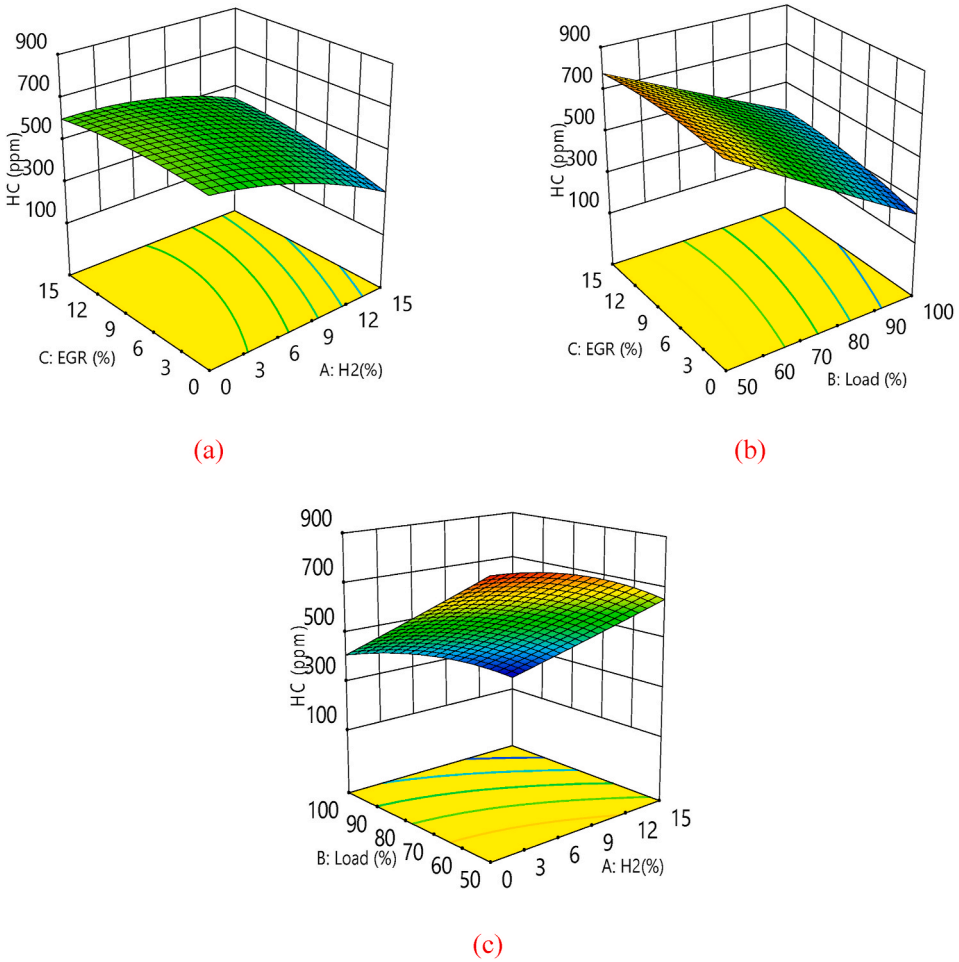

Fig. 20. Surface graphs of the effects of different variables on HC emission. (a) Different EGR rates and H_2 contents on HC; (b) Different EGR rates and load rates on HC; (c) Different load rates and H_2 contents on HC.

4.5. Optimization of optimal solutions

From the above results, it is clear that the ideal solution for performing the optimization is the addition of hydrogen and the use of EGR technology at high loads, which results in the optimal solution for BSFC, NO_x emission, and HC emission. Ultimately, the ideal value of the optimal solution is derived as 0.656, when the corresponding optimal input parameters are 6.92 % hydrogen percentage, 100 % load, and 7.68 % EGR rate, respectively. Fig. 21 shows the contour plots of BSFC, NO_x emission, and HC emission at the highest desired value for the optimized selected solution.

Overall, all three factors have a significant effect on the desired output response, which is statistically significant in reducing BSFC, NO_x emission, and HC emission. Furthermore, the level of EGR rate has a statistically dramatic influence on reducing NO_x emission. The data in Table 8 shows the experimental, predicted, and error ratios of the resulting dual-fuel engine. These data show the errors among the experimental and predicted values of BSFC, NO_x emissions, and HC emission are low, −0.76 %, 3.7 %, and −1.2 %. So the developed response surface model has a high accuracy for the prediction of the dual-fuel engine.

5. Conclusions

In this study, the experimental results of the dual-fuel engine were used to validate a 3D CFD model that was created using the CONVERGE software. Based on the established 3D CFD model, the influence of different EGR and biodiesel-hydrogen blends on the engine was investigated. Finally, a multi-objective optimization of the dual-fuel engine with different loads, hydrogen fractions, and EGR rates was carried out by RSM [58]. These important research findings are summed up as follows.

(1) At 50 %, 75 %, and 100 % loads, increasing the EGR rate of the engine reduces the in-cylinder combustion pressure and the in-cylinder combustion temperature. The higher the EGR rate, the more obvious the effect of reducing the in-cylinder combustion

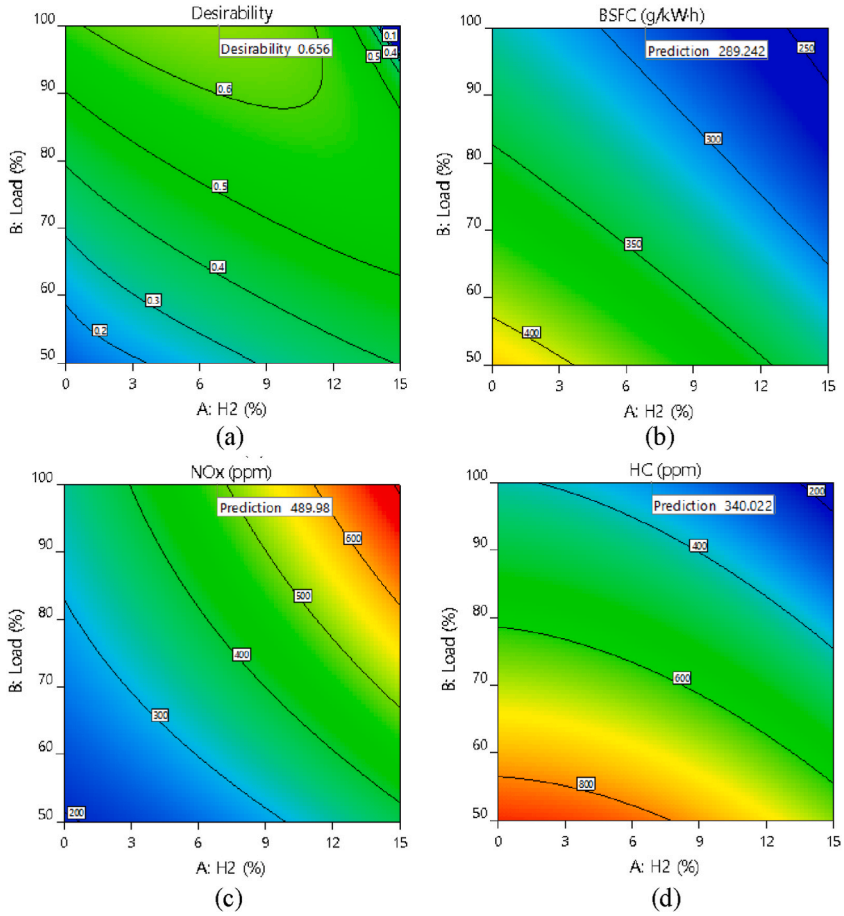

Fig. 21. Statistical plots of load and H_2 fraction versus expectation of desirability (a), BFSC (b), NO_x emission (c), and HC emission (d).

pressure and temperature. However, the EGR technology in the engine will have an impact on the economic characteristics of the engine. Increasing the EGR rate increases the BSFC and decreases the BTE of the engine at all loads.

(2) Increasing the engine EGR rate significantly reduces NO_x emission in the exhaust gas. Compared to the peak NO_x emission at 0 % EGR, the peak NO_x emission at 5 %, 10 %, and 15 % EGR decreased by 27.1 %, 49.5 %, and 65.3 %, respectively. This is due to the deterioration of in-cylinder combustion. However, the rise of the EGR rate leads to a rise in soot, CO, and HC emissions.

(3) The rise in BSFC is significantly impacted by increases in load and hydrogen. While the amount of hydrogen and load decreases, the amount of NO_x emission increases. Furthermore, NO_x emission can be greatly decreased by using EGR technology. The result shows a hydrogen fraction of 6.92 % and an EGR rate of 7.68 % at 100 % load. The ideal value of 0.656 was selected after comprehensive analysis. The optimal BSFC is 288.24 g/kW•h, NO_x emission is 6.9865 g/kW•h, and HC emission is 2.736 g/kW•h, respectively.

To some extent, this study fills the gap in the study of engine characteristics using a simulation method combined with a multi-objective optimization method. In the future, more important parameters will be considered and engine characteristics will be studied using more advanced optimization techniques to achieve better parameter combinations.

6. Data availability statement

Data will be made available on request.

Funding statement

This research is supported by the Natural Science Foundation of Hunan Province under the research grant of 2022JJ50041 and Natural Science Foundation of Hunan Institute of Engineering under the research grant of 23RC033.

This research is supported by the High-level talent research Fund of Yulin Normal University under the research grants of G2018002.

Additional information

No additional information is available for this paper.

CRediT authorship contribution statement

Zhiqing Zhang: Writing – review & editing, Writing – original draft, Methodology, Investigation, Funding acquisition, Data curation. **Hui Liu:** Writing – review & editing, Writing – original draft, Validation, Software, Investigation. **Youchang Li:** Writing – review & editing, Writing – original draft, Methodology, Investigation, Data curation. **Yanshuai Ye:** Writing – original draft, Supervision, Software. **Jie Tian:** Software, Resources, Methodology, Investigation. **Jiangtao Li:** Validation, Software. **Yuejiang Xu:** Software, Resources, Conceptualization. **Junshuai Lv:** Writing – original draft, Investigation, Formal analysis.

Declaration of competing interest

The authors declare that they have no conflict of interests regarding the publication of this paper.

References

[1] O. Awogbemi, D.V. Von Kallon, E.I. Onuh, V.S. Aigbodion, An overview of the classification, production and utilization of biofuels for internal combustion engine applications, Energies 14 (2021) 5687.
[2] P. Tamilselvan, N. Nallusamy, S. Rajkumar, A comprehensive review on performance, combustion and emission characteristics of biodiesel fulled diesel engines, Renewable Sustainable Energy Rev. 79 (2017) 1134–1159.
[3] D. Tan, Y. Meng, J. Tian, C. Zhang, Z. Zhang, G. Yang, et al., Utilization of renewable and sustainable diesel/methanol/n-butanol (DMB) blends for reducing the engine emissions in a diesel engine with different pre-injection strategies, Energy 269 (2023), 126785.
[4] H. Wang, X. Ou, X. Zhang, Mode, technology, energy consumption, and resulting CO_2 emissions in China's transport sector up to 2050, Energy Pol. 109 (2017) 719–733.
[5] B. Zhang, X. Li, Q. Wan, B. Liu, G. Jia, Z. Yin, Hydrocarbon emission control of an adsorptive catalytic gasoline particulate filter during cold-start period of the gasoline engine, Energy 262 (2023), 125445.
[6] Y.-Z. Wang, S. Zhou, X.-M. Ou, Development and application of a life cycle energy consumption and CO_2 emissions analysis model for high-speed railway transport in China, Adv. Clim. Change Res. 12 (2021) 270–280.
[7] B. Zhang, X. Li, Q. Zuo, Z. Yin, J. Zhang, et al., Effects analysis on hydrocarbon light-off performance of a catalytic gasoline particulate filter during cold start, Environ. Sci. Pollut. Control Ser. 29 (2022) 76890–76906.
[8] J. Ye, J.Q. E, Q. Peng, Effects of porosity setting and multilayers of diesel particulate filter on the improvement of regeneration performance, Energy 263 (2023), 126063.
[9] B. Zhang, X. Li, S.H. Tang, Q. Wan, G.H. Jia, B. Liu, S.J. Li, Effects analysis on hydrocarbon removal performance of an adsorptive catalytic gasoline particulate filter in the gasoline engine during cold start, Energy 283 (2023), 128527.
[10] Q. Zhang, X. Qian, R. Li, G. Zhou, Y. Sun, Y. Ma, et al., Explosion characteristics and chemical kinetics of blended LPG/DME clean fuel based on pyrolysis and oxidation mechanism model, Fuel: A Journal of Fuel Science 320 (2022), 123896.
[11] T. Cai, D. Zhao, Enhancing and assessing ammonia-air combustion performance by blending with dimethyl ether, Renew Sust Energ Rev 156 (2022), 112003.
[12] W. Su, P. Liu, C. Cai, H. Ma, B. Jiang, Y. Xing, et al., Hydrogen production and heavy metal immobilization using hyperaccumulators in supercritical water gasification, J. Hazard Mater. 402 (2021), 123541.
[13] O. Balli, H. Caliskan, Energy, exergy, environmental and sustainability assessments of jet and hydrogen fueled military turbojet engine, Int. J. Hydrogen Energy 47 (2022) 26728–26745.
[14] E.G. Varuvel, S. Thiyagarajan, A. Sonthalia, T. Prakash, S. Awad, F. Aloui, et al., Some studies on reducing carbon dioxide emission from a CRDI engine with hydrogen and a carbon capture system, Int. J. Hydrogen Energy 47 (2022) 26746–26757.
[15] B.L. Salvi, K.A. Subramanian, Sustainable development of road transportation sector using hydrogen energy system, Renew. Sustain. Energy Rev. 51 (2015) 1132–1155.
[16] Y. Karagöz, İ. Güler, T. Sandalcı, L. Yüksek, A.S. Dalkılıç, Effect of hydrogen enrichment on combustion characteristics, emissions and performance of a diesel engine, Int. J. Hydrogen Energy 41 (2016) 656–665.
[17] R.L. Patel, C.D. Sankhavara, Biodiesel production from Karanja oil and its use in diesel engine: a review, Renew. Sustain. Energy Rev. 71 (2017) 464–474.
[18] E.J. Liu T, W. Yang, A. Hui, H. Cai, Development of a skeletal mechanism for biodiesel blend surrogates with varying fatty acid methyl esters proportion, Appl. Energy 162 (2016) 278–288.
[19] C.R. Soccol, C.J. Dalmas Neto, V.T. Soccol, E.B. Sydney, E.S.F. Da Costa, A.B.P. Medeiros, et al., Pilot scale biodiesel production from microbial oil of Rhodosporidium toruloides DEBB 5533 using sugarcane juice: performance in diesel engine and preliminary economic study, Bioresour. Technol. 223 (2017) 259–268.
[20] M. Mikulski, K. Duda, S. Wierzbicki, Performance and emissions of a CRDI diesel engine fuelled with swine lard methyl esters–diesel mixture, Fuel 164 (2016) 206–219.
[21] M.S.M. Zaharin, N.R. Abdullah, G. Najafi, H. Sharudin, T. Yusaf, Effects of physicochemical properties of biodiesel fuel blends with alcohol on diesel engine performance and exhaust emissions: a review, Renew. Sustain. Energy Rev. 79 (2017) 475–493.
[22] J. Xue, T.E. Grift, A.C. Hansen, Effect of biodiesel on engine performances and emissions, Renew. Sustain. Energy Rev. 15 (2011) 1098–1116.
[23] G. Knothe, K.R. Steidley, Kinematic viscosity of biodiesel fuel components and related compounds. Influence of compound structure and comparison to petrodiesel fuel components, Fuel 84 (2005) 1059–1065.
[24] S. Murillo, J.L. Míguez, J. Porteiro, E. Granada, J.C. Morán, Performance and exhaust emissions in the use of biodiesel in outboard diesel engines, Fuel 86 (2007) 1765–1771.
[25] Can Ö, Combustion characteristics, performance and exhaust emissions of a diesel engine fueled with a waste cooking oil biodiesel mixture, Energy Convers. Manag. 87 (2014) 676–686.
[26] S.K. Hoekman, C. Robbins, Review of the effects of biodiesel on NO_x emissions, Fuel Process. Technol. 96 (2012) 237–249.
[27] I.K. Hong, J.R. Lee, S.B. Lee, Fuel properties of canola oil and lard biodiesel blends: higher heating value, oxidative stability, and kinematic viscosity, J. Ind. Eng. Chem. 22 (2015) 335–340.
[28] B.R. Moser, Fuel property enhancement of biodiesel fuels from common and alternative feedstocks via complementary blending, Renew. Energy 85 (2016) 819–825.
[29] I. Dincer, C. Acar, Review and evaluation of hydrogen production methods for better sustainability, Int. J. Hydrogen Energy 40 (2015) 11094–11111.
[30] R.K. Maurya, M.R. Saxena, Characterization of ringing intensity in a hydrogen-fueled HCCI engine, Int. J. Hydrogen Energy 43 (2018) 9423–9437.

[31] M. Vijayaragavan, B. Subramanian, S. Sudhakar, L. Natrayan, Effect of induction on exhaust gas recirculation and hydrogen gas in compression ignition engine with simarouba oil in dual fuel mode, Int. J. Hydrogen Energy 47 (2022) 37635–37647.
[32] D. Tan, Y. Wu, J. Lv, J. Li, X. Ou, Y. Meng, G. Lan, Y. Chen, Z. Zhang, Performance optimization of a diesel engine fueled with hydrogen/biodiesel with water addition based on the response surface methodology, Energy 263 (3) (2023), 125869.
[33] Z. Weidong, Y. Jiangwei, Z. Xiaoyin, Q. Xiaolong, Review on the progress of the first-generation biodiesel hydrogenation and upgrading, Energy Sources, Part A Recovery, Util. Environ. Eff. 42 (2020) 2704–2714.
[34] A. Maiboom, X. Tauzia, J.-F. Hétet, Experimental study of various effects of exhaust gas recirculation (EGR) on combustion and emissions of an automotive direct injection diesel engine, Energy 33 (2008) 22–34.
[35] W. Zhao, S. Mi, H. Wu, Y. Zhang, Q. Zhang, Z. He, et al., Towards a comprehensive understanding of mode transition between biodiesel-biobutanol dual-fuel ICCI low temperature combustion and conventional CI combustion - part I: characteristics from medium to high load, Energy 246 (2022), 123414.
[36] H. Yokomura, S. Kouketsu, S. Kotooka, Y. Akao. Transient EGR control for a turbocharged heavy duty diesel engine, SAE Technical Paper Series, 2004, https://doi.org/10.4271/2004-01-0120.
[37] D.W. Dickey, T.W. Ryan, A.C. Matheaus, NOx control in heavy-duty diesel engines - what is the limit? International Congress & Exposition (1998), 980147.
[38] B.R. Kumar, S. Saravanan, Effect of exhaust gas recirculation (EGR) on performance and emissions of a constant speed DI diesel engine fueled with pentanol/diesel blends, Fuel 160 (2015) 217–226.
[39] Z. Zhang, J. Tian, J. Li, J. Lv, S. Wang, Y. Zhong, R. Dong, S. Gao, C. Cao, D. Tan, Investigation on combustion, performance and emission characteristics of a diesel engine fueled with diesel/alcohol/n-butanol blended fuels, Fuel 320 (2022), 123975.
[40] Y. Chen, J. Zhang, Z. Zhang, W. Zhong, Z. Zhao, J. Hu, Utilization of renewable biodiesel blends with different proportions for the improvements of performance and emission characteristics of a diesel engine, Heliyon (2023), e19196.
[41] Z. Han, R.D. Reitz, Turbulence modeling of internal combustion engines using RNG κ-ε models, Combust. Sci. Technol. 106 (1995) 267–295.
[42] Z. Zhang, J. Lv, G. Xie, S. Wang, Y. Ye, G. Huang, D. Tan, Effect of assisted hydrogen on combustion and emission characteristics of a diesel engine fueled with biodiesel, Energy 254 (2022), 124269.
[43] A.B. Liu, D.K. Mather, R.D. Reitz, Modeling the Effects of Drop Drag and Breakup on Fuel Sprays, SAE Technical Paper Series, 1993, 930072.
[44] J.C. Beale, R.D. Reitz, Modeling spray atomization with the Kelvin-Helmholtz/Rayleigh-Taylor hybrid model, Atomization Sprays 9 (1999) 623–650.
[45] J. Xin, L. Ricart, R.D. Reitz, Computer modeling of diesel spray atomization and combustion, Combust. Sci. Technol. 137 (1998) 171–194.
[46] A.A. Amsden, P.J. O'Rourke, T.D. Butler, KIVA-II: A Computer Program for Chemically Reactive Flows with Sprays, Los Alamos National Lab. (LANL), Los Alamos, NM (United States), 1989, 6228444.
[47] Z. Han, R.D. Reitz, A temperature wall function formulation for variable-density turbulent flows with application to engine convective heat transfer modeling, Int. J. Heat Mass Tran. 40 (1997) 613–625.
[48] Z. Zhang, J. Li, J. Tian, R. Dong, Z. Zou, S. Gao, D. Tan, Performance, combustion and emission characteristics investigations on a diesel engine fueled with diesel/ethanol/n-butanol blends, Energy 249 (2022), 123733.
[49] Y. Sun, R.D. Reitz, Modeling diesel engine NO_x and soot reduction with optimized two-stage combustion, SAE Technical Paper Series (2006) doi:10.4271/2006-01-0027.
[50] Y. Wang, X. Wang, J. Pan, H. Wei, X. Zhou, M. Pan, Effects of different injection strategies on mixing, combustion and emission behavior of gasoline compression ignition (GCI) engines, Fuel: A Journal of Fuel Science 317 (2022), 123486.
[51] Z. Zhang, E.J. Deng Y, M. Pham, W. Zuo, Q. Peng, et al., Effects of fatty acid methyl esters proportion on combustion and emission characteristics of a biodiesel fueled marine diesel engine, Energy Convers. Manag. 159 (2018) 244–253.
[52] Z. Zhang, J. Tian, G. Xie, J. Li, W. Xu, F. Jiang, et al., Investigation on the combustion and emission characteristics of diesel engine fueled with diesel/methanol/n-butanol blends, Fuel 314 (2022), 123088.
[53] Z. Zhang, J. Ye, D. Tan, Z. Feng, Y. Huang, The effects of Fe_2O_3 based DOC and SCR catalyst on the combustion and emission characteristics of a diesel engine fueled with biodiesel, Fuel 290 (2021), 120039.
[54] X. Jiang, H. Wei, L. Zhou, R. Chen, Numerical study on the effects of multiple-injection coupled with EGR on combustion and NO_x emissions in a marine diesel engine, Energy Proc. 158 (2019) 4429–4434.
[55] X. Duan, Z. Xu, X. Sun, B. Deng, J. Liu, Effects of injection timing and EGR on combustion and emissions characteristics of the diesel engine fuelled with acetone–butanol–ethanol/diesel blend fuels, Energy 231 (2021), 121069.
[56] S. Saravanan, G.L.N. Rao, Effect of EGR on performance and emission characteristics of diesel engine at advanced injection timing, Int. J. Oil Gas Coal Technol. 7 (2014) 335–345.
[57] O.I. Awad, R. Mamat, O.M. Ali, W.H. Azmi, K. Kadirgama, I.M. Yusri, et al., Response surface methodology (RSM) based multi-objective optimization of fusel oil-gasoline blends at different water content in SI engine, Energy Convers. Manag. 150 (2017) 222–241.
[58] Z. Zhang, J. Li, J. Tian, Y. Zhong, Z. Zou, R. Dong, S. Gao, W. Xu, D. Tan, The effects of Mn-based catalysts on the selective catalytic reduction of NO_x with NH_3 at low temperature: a review, Fuel Process. Technol. 230 (2022), 107213.